Modelling size-fractionated primary production in the Atlantic Ocean from remote sensing

Robert J.W. Brewin[*,a,b], Gavin H. Tilstone[a], Thomas Jackson[a], Terry Cain[a], Peter I. Miller[a], Priscila K. Lange[c], Ankita Misra[d], Ruth Airs[a]

[a]*Plymouth Marine Laboratory (PML), Prospect Place, The Hoe, Plymouth PL1 3DH, UK*
[b]*National Centre for Earth Observation, PML, Plymouth PL1 3DH, UK*
[c]*Department of Earth Sciences, University of Oxford, Parks Road, Oxford OX1 3PR, UK*
[d]*Indian Institute of Technology, Bombay, Powai, Mumbai 400 076, Maharashtra, India*

Abstract

Marine primary production influences the transfer of carbon dioxide between the ocean and atmosphere, and the availability of energy for the pelagic food web. Both the rate and the fate of organic carbon from primary production are dependent on phytoplankton size. A key aim of the Atlantic Meridional Transect (AMT) programme has been to quantify biological carbon cycling in the Atlantic Ocean and measurements of total primary production have been routinely made on AMT cruises, as well as additional measurements of size-fractionated primary production on some cruises. Measurements of total primary production collected on the AMT have been used to evaluate remote-sensing techniques capable of producing basin-scale estimates of primary production. Though models exist to estimate size-fractionated primary production from satellite data, these have not been well validated in the Atlantic Ocean, and have been parameterised using measurements of phytoplankton pigments rather than direct measurements of phytoplankton size structure. Here, we re-tune a remote-sensing primary production model to estimate production in three size fractions of phytoplankton

(<2μm, 2-10μm and >10μm) in the Atlantic Ocean, using measurements of size-fractionated chlorophyll and size-fractionated photosynthesis-irradiance experiments conducted on AMT 22 and 23 using sequential filtration-based methods. The performance of the remote-sensing technique was evaluated using: (i) independent estimates of size-fractionated primary production collected on a number of AMT cruises using ^{14}C on-deck incubation experiments; and (ii) Monte Carlo simulations. Considering uncertainty in the satellite inputs and model parameters, we estimate an average model error of between 0.27 and 0.63 for $\log_{10}$-transformed size-fractionated production, with lower errors for the small size class (<2μm), higher errors for the larger size classes (2-10μm and >10μm), and errors generally higher in oligotrophic waters. Application to satellite data in 2007 suggests the contribution of cells <2μm and >2μm to total primary production is approximately equal in the Atlantic Ocean.

Key words: Phytoplankton, Primary Production, Size, Ocean colour, Remote sensing, Atlantic Ocean

1. Introduction

Primary production is the conversion of inorganic carbon (carbon dioxide) to organic carbon (e.g., glucose). It occurs mainly through the process of photosynthesis, using light as an energy source. Approximately half of net primary production on Earth can be attributed to phytoplankton (Longhurst et al., 1995; Field

*Corresponding author. Plymouth Marine Laboratory (PML), Prospect Place, The Hoe, Plymouth PL1 3DH, UK

Email address: robr@pml.ac.uk (Robert J.W. Brewin)

et al., 1998). Primary production by phytoplankton modifies the total CO_2 concentration in seawater, influencing CO_2 air-sea gas exchange and consequently Earth's climate. Nearly all marine life is directly or indirectly reliant on the organic carbon produced by phytoplankton as an energy source. The magnitude of primary production has been found to impact global fish catch (Chassot et al., 2010). It is for these reasons that a core goal of the Atlantic Meridional Transect (AMT) programme has been to measure primary production by phytoplankton in the Atlantic Ocean (Marañón and Holligan, 1999; Marañón et al., 2000, 2001; Aiken et al., 2000; Robinson et al., 2002; Fernández et al., 2003; Robinson et al., 2006; Poulton et al., 2006; Tilstone et al., 2009, Accepted).

Since the advent of satellite remote-sensing of ocean colour, synoptic estimations of primary production across entire ocean basins has been attainable, through the implementation of established and proven primary production models (e.g., Platt et al., 1980, 1990; Platt and Sathyendranath, 1993). Primary production (P) can be expressed using an available light model, such that

$$P = BP_m^B(1 - \exp(-\frac{\alpha^B I}{P_m^B})), \tag{1}$$

where B is an index of the phytoplankton biomass, taken here to be the concentration of chlorophyll-a pigments, P_m^B is the assimilation number of the light-saturation curve (maximum photosynthetic rate normalised by biomass in the absence of photoinhibition), α^B is the initial slope measured for a flat incident spectral light field in the photosynthetically-active domain (about 400 to 700 nm), and I is the total available irradiance (photosynthetically available radia-

tion, denoted PAR). Though not stated explicitly in Eq. 1, all these components are depth-dependent. For simplicity we have not included in Eq. 1 the effect of photoinhibition, which can occur in nature (Platt et al., 1980). Non-spectral, available light models (Eq. 1) deal with total light (PAR), without taking into account the spectral selectivity in absorption and utilisation of light available for photosynthesis (unlike some spectral approaches e.g., Platt and Sathyendranath, 1988; Sathyendranath and Platt, 1989; Morel, 1991; Smyth et al., 2005). If the parameters of the non-spectral models are not selected in an appropriate manner this can lead to errors in computation of primary production (Kyewalyanga et al., 1992). Whereas there are other methods of expressing P to that shown in Eq. 1, all approaches are fundamentally consistent and are all based on a key set of parameters (Sathyendranath and Platt, 2007).

Acknowledging assumptions about vertical and daily variation, two key variables in Eq. 1 are retrievable from satellite data, namely the concentration of chlorophyll-a pigments (B) and the total available irradiance (I). Therefore, to produce synoptic estimates of primary production using satellite data (B and I) and Eq. 1, one needs a methodology to assign appropriate values for P_m^B and α^B. Two approaches commonly used include: (i) assigning P_m^B and α^B based on an extensive *in situ* dataset, either partitioned into regional and seasonal categorises, typically conducted using biogeographical provinces (Longhurst et al., 1995; Sathyendranath et al., 1995), or interrogated using statistical methods such as nearest-neighbour together with spatial and temporal information and satellite data (Platt et al., 2008); and (ii) tying P_m^B and α^B directly and continuously to

one (or more) environmental variable retrievable from satellite data, such as sea-surface temperature, irradiance and chlorophyll (Eppley, 1972; Behrenfeld and Falkowski, 1997; Sathyendranath et al., 2009; Saux Picart et al., 2014).

In recent years, a third approach to model variations in P_m^B and α^B has been suggested, which incorporates information on phytoplankton size structure (Claustre et al., 2005; Mouw and Yoder, 2005; Uitz et al., 2008). In this approach, size-fractionated chlorophyll biomass is inferred from satellite data (e.g. Uitz et al., 2006) and used together with predetermined P_m^B and α^B values assigned to each size class and forced with total available irradiance (e.g. Uitz et al., 2008), to estimate size-fractionated primary production which is then summed to give total primary production (e.g. Silió-Calzada et al., 2008; Uitz et al., 2008, 2009, 2010, 2012). In addition to capturing variations in P_m^B and α^B, this approach can also provide group-specific (according to size) primary production. Considering cell size influences many key processes in biogeochemisty and marine ecology (Chisholm, 1992; Marañón, 2009, 2015; Finkel et al., 2010), such as the export of carbon (Laws et al., 2000; Guidi et al., 2009; Briggs et al., 2011) and the transfer of energy through the marine food chain (Maloney and Field, 1991; Legendre and LeFevre, 1991), such an approach offers a more holistic route to understanding marine ecosystems (Le Quéré et al., 2005; Hirata et al., 2009) and is consistent with many marine biogechemistry models that use a size-based partitioning for phytoplankton (Aumont et al., 2003; Blackford et al., 2004; Kishi et al., 2007; Marinov et al., 2010; Ward et al., 2012).

Yet, current approaches for estimating size-fractionated primary production

were parameterised using information on phytoplankton size structure inferred indirectly from phytoplankton pigments (Uitz et al., 2006, 2008) derived from High Performance Liquid Chromatography (HPLC), and not from direct measurements of phytoplankton size. Whereas size-fractionated chlorophyll inferred from HPLC data correlates well with that derived using methods that explicitly partition the size classes (such as sequential size-fractionated filtration), significant biases between the two methods have been observed along the Atlantic Meridional Transect (Brewin et al., 2014b), with implications for models that estimate size-fractionated chlorophyll (Brewin et al., 2014c) and size-fractionated primary production from remote sensing.

On AMT cruises 22 and 23, which took place between October and November 2012 and 2013 respectively, sequential size-fractionated chlorophyll and phytosynthesis-irradiance experiments were conducted (Tilstone et al., Accepted) and used to estimate size-specific P_m^B, α^B and B. In this paper, we re-parameterise a size-fractionated primary production model using these direct measurements. The model is evaluated using independent measurements of total and size-fractionated primary production, collected on a variety of AMT cruises, and Monte Carlo simulations. The model is then used to provide synoptic estimates of size-fractionated primary production in the Atlantic Ocean for 2007, and results are compared with previous studies. Finally, we discuss advantages and disadvantages of the technique and routes to future improvement.

2. Methodology

Using an available light model (Platt et al., 1980) that considers three size classes of phytoplankton (Uitz et al., 2008), we express size-fractionated primary production as

$$P = \int_{t=0}^{D} \int_{z=0}^{1.5Z_p} \sum_{i=1}^{3} B_i(z) P^B_{m,i}(z)[1 - \exp(-\frac{\alpha^B_i(z) I(z,t)}{P^B_{m,i}(z)})] dz dt, \quad (2)$$

where D is day length, Z_p is the euphotic depth (1 % light level, where $1.5Z_p$ represents the 0.1 % light level), z is depth and t is time. The subscript i refers to the three size classes of phytoplankton, where $i = 1$ refers to cells $<2\,\mu$m (pico-phytoplankton, referred to here as small cells), $i = 2$ cells 2-10 μm (referred to here as medium cells), and $i = 3$ cells $>10\,\mu$m (referred to here as large cells). Table 1 defines all symbols used in the paper. Note that size ranges of medium and large cells differ slightly from those of Uitz et al. (2008), who used the 2-20 μm and $>20\,\mu$m size classes. We used the $10\,\mu$m (rather than $20\,\mu$m) partitioning as phytoplankton cells rarely exceed $20\,\mu$m over much of the AMT cruise tracks, and thus data were collected using $10\,\mu$m polycarbonate filter pads rather than $20\,\mu$m. Equation 2 builds on a two-component model of primary production proposed by Brewin et al. (2010a).

The following sections describe how we parameterised each component of Eq. 2. We begin each section by describing the datasets used to parameterise each component, followed by the equations used for parameterisation, and finalise each section by providing a list of model parameters and an evaluation of our approach to modelling each component, relative to existing techniques.

126 *2.1. Day length (D)*

127 Day length (D) was estimated as a simple function of latitude and day of year
128 (DOY) following the Schoolfield model, as defined in Eq. 1-3 of Forsythe et al.
129 (1995).

130 *2.2. Euphotic depth (Z_p)*

131 The euphotic depth (Z_p) was estimated at 37 stations on the AMT 22 cruise
132 and 21 stations on the AMT 23 cruise. These stations were sampled around local
133 noon. The depth of the 1 % light level (Z_p) and the average diffuse attenuation
134 coefficient in the euphotic layer (K_{Zp}) were extracted at each station using ver-
135 tical profiles of photosynthetically available radiation (PAR) measured using a
136 Chelsea MKI Fast Repitition Rate Fluorometer (FRRF) on AMT 22 and a Bio-
137 spherical PAR irradiance sensor on AMT 23, and assuming Beer-Lambert Law.
138 For each station, discrete water samples (1-4 L) were collected in the surface
139 layer (z ~2-5 m). The water samples were filtered onto Whatman GF/F glass
140 microfibre filter pads (~0.7μm), flash frozen in liquid nitrogen and transferred
141 to the -80°C freezer. Total surface chlorophyll-a concentration (B_s, the sum of
142 key photosynthetic pigment concentrations including monovinyl chlorophyll-a,
143 divinyl chlorophyll-a, and chlorophyllide-a) were determined after each cruise in
144 the laboratory using HPLC analysis (see section 2.3.1 for further details). Here
145 we define B_s as the concentration in the upper mixed-layer (Z_m), which rarely is
146 less than 10 m (de Boyer Montégut et al., 2004).

147 Satellite ocean-colour data can provide estimates of total chlorophyll-a con-
148 centration within the 1st optical depth, which can vary from <1 to 40 m depth.

Comparisons of satellite estimates with *in situ* data collected at 5 m along two AMT cruise tracks (AMT 19 and 22) show very good agreement (Brewin et al., 2016). Therefore, we made the assumption that satellite ocean-colour data provides surface chlorophyll-a concentration (B_s). To estimate Z_p using satellite ocean-colour data for use in Eq. 2 we used the approach of Morel et al. (2007), relating empirically Z_p to B_s according to

$$Z_p = 10^{[q_a + q_b \log_{10}(B_s) + q_c \log_{10}(B_s)^2 + q_d \log_{10}(B_s)^3]}, \quad (3)$$

where q_a, q_b, q_c and q_d are empirical parameters. Equation 3 was re-parameterised using Z_p and B_s data from AMT 22 and 23. Values of the coefficients are provided in Table 2 and Eq. 3 is plotted in Fig. 1a together with the parameters from Morel et al. (2007). In general the re-tuned algorithm is in good agreement with that of the global model of Morel et al. (2007), but departs at chlorophyll concentrations less than 0.1 mg m^{-3}, with slightly higher estimates of Z_p compared with Morel et al. (2007). Equation 3, together with values of q_a, q_b, q_c and q_d (Table 2), was used to estimate Z_p from satellite estimates of B_s for input into Eq. 2.

2.3. Size-fractionated biomass B_i

The total chlorophyll-a concentration (B) is used here as an index of phytoplankton biomass. For Eq. 2 we require $B_i(z)$, vertical variations (z) in the chlorophyll-a concentration (B) of three size classes (i = small (1), medium (2) and large cells (3)), down to a depth of $1.5 \times Z_p$. To get $B_i(z)$ for Eq. 2, we first

estimate $B(z)$ from B_s (available from satellite ocean-colour data), then estimate $B_t(z)$ from $B(z)$.

2.3.1. Vertical variations in total chlorophyll (B)

To estimate the chlorophyll profile in the Atlantic Ocean we made use of vertical profiles of HPLC total chlorophyll data collected on AMT cruises 1-22. For all cruises, between 1 and 4 L of seawater were filtered onto Whatman GF/F glass microfibre filter pads (~0.7μm), flash frozen in liquid nitrogen and transferred to the -80°C freezer. If liquid nitrogen was not available the filters were transferred directly to the -80°C freezer. Samples were extracted under dim light conditions on ice, in 2 mL 90% acetone by sonication (Sonics Vibracell probe, 35 s, 40 W), followed by a soaking period (total extraction time of 1 h). Extracts were clarified by centrifugation. For additional details on sample analysis for total chlorophyll (B), see Aiken et al. (2009) and Airs and Martinez-Vicente (2014a,b,c). For each profile, estimates of mixed-layer depth (Z_m) were extracted from a monthly climatology (de Boyer Montégut et al., 2004, based on a temperature criterion of ±0.2 degree difference from the temperature at 10 m depth) using a simple latitude and longitude match-up technique, and euphotic depth (Z_p) was estimated from B_s using Eq. 3. The ratio of the euphotic depth (Z_p) to the mixed-layer depth (Z_m) was computed for each profile.

For our primary production model, we assumed a non-uniform vertical chlorophyll profile in stratified conditions and a uniform profile in mixed waters, following Morel and Berthon (1989) and Uitz et al. (2006). The non-uniform vertical chlorophyll profile was modelled using a shifted Gaussian model adapted

from Platt and Sathyendranath (1988) and Uitz et al. (2006). As with Uitz et al. (2006), the non-uniform profile was computed based on two dimensionless quantities, the dimensionless depth (ζ), where $\zeta = z/Z_p$, and a normalised chlorophyll profile. However, unlike Uitz et al. (2006) who normalised the chlorophyll profile by the average chlorophyll concentration within the euphotic layer, here we normalise the chlorophyll profile ($B^{B_s}(\zeta)$) by the surface chlorophyll concentration (B_s), such that $B^{B_s}(\zeta) = B(\zeta)/B_s$. After this double normalisation has been applied, the dimensionless chlorophyll profile ($B^{B_s}(\zeta)$) was expressed as

$$B^{B_s}(\zeta) = 1 - S^{B_s}\zeta + B_m^{B_s} \exp\{-[(\zeta - \zeta_m)/\sigma]^2\}, \quad (4)$$

where S^{B_s} represents a background linear decrease with ζ, $B_m^{B_s}$ the maximum value of $B^{B_s}(\zeta)$, ζ_m the dimensionless depth at which $B_m^{B_s}$ occurs, and σ the width of the $B_m^{B_s}$ peak. There are four unknown parameters in Eq. 4: S^{B_s}, $B_m^{B_s}$, ζ_m and σ, given that the normalised surface value is equal to one in Eq. 4. Two different approaches have been presented to assign parameters of shifted Gaussian models at large scales: assigning parameters based on season and region (e.g. biogeochemical provinces; Platt and Sathyendranath, 1991; Sathyendranath et al., 1995; Longhurst et al., 1995); or tying parameters to trophic categories, typically using boundaries in B_s (Morel and Berthon, 1989; Uitz et al., 2006). Here we investigated the relationship between model parameters and surface chlorophyll concentration B_s, with the goal of estimating model parameters in Eq. 4 as continuous functions of B_s.

Equation 4 was fitted to 112 HPLC AMT chlorophyll profiles in stratified

environments (where $Z_p/Z_m > 1.0$), using a non-linear least-square method (Levenberg-Marquardt, IDL Routine MPFITFUN (Moré, 1978; Markwardt, 2008)). Profiles were used only from stratified environments (where $Z_p/Z_m > 1.0$), where measurements were made in the surface layer (<10 m), with a minimum of five samples in the profile, and where Eq. 4 explained 96% of the variability in the data. The last constraint was to avoid the impact of any uncharacteristic profiles, possibly caused by measurement error, on the fitting of Eq. 4 to individual profiles. Retrieved parameters are plotted as a function of B_s in Fig. 2. Of the four parameters, $B_m^{B_s}$ and ζ_m were significantly correlated with B_s ($p < 0.05$), with S^{B_s} and σ relatively constant over a range of B_s (Fig. 2). Therefore, we fixed S^{B_s} and σ at 0.325 and 0.295 respectively (Table 2), and $B_m^{B_s}$ was modelled as a function of B_s according to $B_m^{B_s} = 10^{(\log_{10}(B_s)E+F)}$ ($r = 0.75$, $p < 0.001$) and ζ_m as a function of B_s according to $\zeta_m = \log_{10}(B_s)G+H$ ($r = 0.24$, $p = 0.010$). Parameter values for E, F, G and H are provided in Table 2. Figure 3a illustrates how $B^{B_s}(\zeta)$ varies with B_s for stratified environments, and Fig. 3b shows the reconstructed total chlorophyll ($B(z)$).

For mixed environments, we made the assumption of a uniform profile (Uitz et al., 2006), such that $B(z) = B_s$. Rather than using a binary change from mixed to stratified waters, based on Z_p/Z_m being greater than or less than 1.0, we introduced a smooth transition from mixed to stratified waters, where $B(z)$ was

modelled according to

$$B(z) = \begin{cases} B_s & \text{if } Z_p/Z_m < 1.0 \\ \xi([1 - S^{B_s}\zeta + B_m^{B_s} \exp\{-[(\zeta - \zeta_m)/\sigma]^2\}]B_s) + (1 - \xi)B_s & \text{if } Z_p/Z_m \geq 1.0 \text{ and } \leq 1.5 \\ [1 - S^{B_s}\zeta + B_m^{B_s} \exp\{-[(\zeta - \zeta_m)/\sigma]^2\}]B_s & \text{if } Z_p/Z_m > 1.5, \end{cases} \quad (5)$$

where ξ serves to provide a linear transition from mixed to stratified waters as Z_p/Z_m increases from 1.0 to 1.5. This parameter is computed as $\xi = (Z_p/Z_m - 1.0)/(1.5 - 1.0)$. Figure 3c shows $B(z)$ where $B_s = 0.1$ as a function of Z_p/Z_m, to illustrate the change in profile from stratified to mixed waters. Figure 5 shows integrated chlorophyll, computed by vertical integration of Eq. 5, as a function of surface chlorophyll (B_s) and Z_p/Z_m. Results are consistent with empirical equations of Uitz et al. (2006) based on a global dataset, with integrated chlorophyll increasing as a function of total chlorophyll, and the slopes varying between stratified and mixed waters. For stratified conditions, over the range of 0.01 to 1.0 mg m^{-3} chlorophyll (i.e. typical conditions encountered on an AMT cruise), the model is in good agreement with the empirical equations of Uitz et al. (2006).

As a qualitative verification of Eq. 5 we estimated $B(z)$ using satellite B_s as input (monthly chlorophyll composites from ESA OC-CCI data, see section 2.7.1 for details on satellite data) and mixed-layer from a monthly climatology (de Boyer Montégut et al., 2004) for October 2008 and November 2010. They

are compared with chlorophyll estimated from an *in vivo* fluorometer on a CTD during the AMT 18 cruise (4th October to 10th November 2008) and AMT20 cruise (12th October to 25th November 2010), deployed at discrete stations along the cruise track (Fig. 5). In general, Eq. 5 captures the vertical variations in B along both transects. Equation 5 was used to estimate $B(z)$ with B_s, Z_p and Z_m as input, and parameters are provided in Table 2.

2.3.2. Size-fractionated chlorophyll (B)

Having obtained $B(z)$, next we estimate $B_i(z)$ from $B(z)$. During AMT 13, 14, 22 and 23 cruises, ~200-300 ml water samples were sequentially filtered through different-sized polycarbonate filters. All four cruises incorporated a 10 μm, 2 μm and 0.2 μm partitioning. During AMT 22 and 23 cruises, water samples were collected at the surface (<5 m) and also the sub-surface maxima ($\sim \zeta_m$), whereas AMT cruises 13 and 14 water samples were collected at a variety of depths. After filtration, pigments were extracted by storing the filters in 90% acetone at -20°C between 10 and 24 hrs (Marañón et al., 2001; Brewin et al., 2014c). A Turner Design Fluorometer (either 10 AU, TD-700 or Trilogy) was used to derive the chlorophyll concentration of three size classes (small cells <2 μm (B_1), medium cells 2-10 μm (B_2), and large cells >10 μm (B_3)). For each cruise, the fluorometer was pre- and post-calibrated with pure chlorophyll-a as a standard. Figure 6 shows the geographical distribution of samples for each cruise. Data from AMT 22 and 23 cruises were used for model development, and data from AMT 13 and 14 cruises for independent evaluation of the model.

To estimate $B_i(z)$ from $B(z)$, we used the three-component model of Brewin

et al. (2010b) to estimate size-fractionated chlorophyll (B_i) as a function of total chlorophyll (B). The model is based on two exponential functions (Sathyendranath et al., 2001), where the chlorophyll concentration of combined small- and medium cells ($B_{1,2}$, cells $<10\,\mu$m) and small cells (B_1, cells $<2\,\mu$m) can be expressed as

$$B_{1,2} = B^m_{1,2}[1 - \exp(-S_{1,2}B)], \tag{6}$$

and

$$B_1 = B^m_1[1 - \exp(-S_1 B)]. \tag{7}$$

The parameters $B^m_{1,2}$ and B^m_1 are the asymptotic maximum values for the associated size classes ($<10\,\mu$m and $<2\,\mu$m respectively): $S_{1,2}$ and S_1 determine the increase in size-fractionated chlorophyll ($<10\,\mu$m and $<2\,\mu$m respectively) with increasing total chlorophyll (B). Although the model of Brewin et al. (2010b) was originally developed for slightly different size fractions ($<20\,\mu$m and $<2\,\mu$m), recent work has shown it holds for multiple size fractions between 2 and $20\,\mu$m (Brewin et al., 2014c). The chlorophyll concentration of medium cells (B_2) and large cells (B_3) can be calculated according to

$$B_2 = B_{1,2} - B_1, \tag{8}$$

and

$$B_3 = B - B_{1,2}. \quad (9)$$

Equations 6 and 7 were fitted to B, $B_{1,2}$ and B_1 from AMT cruises 22 and 23 (Levenberg-Marquardt, IDL Routine MPFITFUN (Moré, 1978; Markwardt, 2008)). To avoid the undue influence of large chlorophyll values on the parameterisation of the model, the fitting procedure was applied to $\log_{10}$-transformed data. Parameter values for $B^m_{1,2}$, B^m_1, $S_{1,2}$ and S_1 are provided in Table 2. Values were found to be similar to those estimated by Brewin et al. (2014c, $B^m_{1,2} = 1.60$, $B^m_1 = 0.66$, $S_{1,2} = 0.56$ and $S_1 = 1.20$) developed using size-fractionated filtration data independent to that of AMT 22 and 23 cruises.

Figure 6 shows size-fractionated chlorophyll plotted as a function of total chlorophyll for AMT 22 and 23 cruises, with the Brewin et al. (2010b) model overlain. The model is seen to capture the relationships in the AMT 22 and 23 data. The Brewin et al. (2010b) model also compares well with independent size-fractionated chlorophyll from AMT 13 and 14 (Fig. 6, when applying the model (Eq. 6-9) to the total chlorophyll concentration (B)). There were no significant differences in model parameters between the surface and sub-surface maximum data (parameters overlapped at the 95 % confidence interval). Equations 6-9 were used to estimated $B_i(z)$ from $B(z)$, and parameters are provided in Table 2. For our production model (Eq. 2), size-fractionated biomass ($B_i(z)$) was assumed to be constant over daylength (D).

2.4. *Phytoplankton size-specific photophysiology ($P^B_{m,i}$ and α^B_i)*

Photosynthesis-irradiance experiments were conducted at 36 stations on AMT 22 and 26 stations on AMT 23, at two depths in the water column (surface (<5 m) and the sub-surface maxima ($\sim \zeta_m$)). The experiments were run in photosynthetrons illuminated by 35 or 50 W tungsten halogen lamps for surface samples when ambient irradiance was >800μmol m^{-2} s^{-1}, and using 9 W LEDs for the sub-surface samples and for surface samples when ambient irradiance was <800μmol m^{-2} s^{-1}, following Tilstone et al. (2003). Each incubator housed 15 sub-samples in 60 mL polycarbonate bottles which were inoculated with between 185 and 370 kBq (5-10 μCi) of ^{14}C labelled bicarbonate. The samples were maintained at *in situ* temperature using the ship's non-toxic seawater supply for the surface samples and at ambient temperature at the surface maxima ($\sim \zeta_m$) with a Polyscience chiller. After 1 to 2 h of incubation, the suspended material was sequentially filtered though 10 μm, 2 μm and 0.2 μm polycarbonate filters to measure size-specific phytoplankton photosynthetic rates. The filters were exposed to concentrated HCl fumes for 12 h, immersed in scintillation cocktail and ^{14}C disintegration per minute (DPM) was measured on board using a Packard Tricarb 2900 liquid scintillation counter, and the external standard and the channel ratio methods to correct for quenching. Dark bottle incubations were used to obtain blank DPMs which were subtracted from the light bottle DPMs. Production for each size class P_i was then normalised by concurrent measurements of chlorophyll biomass in each size class B_i (see section 2.3.2), to give normalised size-fractionated production P^B_i.

330 The broadband light-saturated chlorophyll-specific rate of photosynthesis for
331 each size class ($P^B_{m,i}$) and the initial slope of the photosynthesis-irradiance curve
332 (α^B_i) were then estimated by fitting the model of Platt et al. (1980) to the nor-
333 malised size-fractionated production data. For each station Z_p was extracted (see
334 section 2.2) and ζ computed (z/Z_p). Values of α^B_i are biased due to the emission
335 spectrum of the light source. The bias was corrected by multiplying each α^B_i
336 value by a factor W_i (Kyewalyanga et al., 1997), computed as

$$W_i = \frac{\bar{a}_{p,i}}{\bar{a}_{T,i}}, \tag{10}$$

337 where $\bar{a}_{p,i}$ is the unweighted mean absorption spectrum and $\bar{a}_{T,i}$ is the weighted
338 mean absorption spectrum of each size class of phytoplankton (i). These were
339 computed according to

$$\bar{a}_{p,i} = \frac{\int_{\lambda=400}^{700} a^B_{p,i}(\lambda) B_i}{300} d\lambda, \tag{11}$$

340 and

$$\bar{a}_{T,i} = \frac{\int_{\lambda=400}^{700} a^B_{p,i}(\lambda) B_i I_T(\lambda)}{\int_{\lambda=400}^{700} I_T(\lambda)} d\lambda, \tag{12}$$

341 where $I_T(\lambda)$ is the spectral irradiance of the lamp used (either tungsten halogen
342 or LED lamp, depending on sample), and $a^B_{p,i}(\lambda)$ is the chlorophyll-specific ab-
343 sorption coefficient of each size class (small, medium and large), which we took
344 from Uitz et al. (2008) and varied with ζ (see Eq. 13 of Uitz et al., 2008). Only

photosynthesis-irradiance curves for which $P^B_{m,i}$ and α^B fell within realistic natural values ($0.2 < P^B_{m,i} < 25$ and $0.005 < \alpha^B_i < 0.2$) and for which there were concurrent data on Z_p were used.

Both $P^B_{m,i}$ and α^B_i were modelled using the approach of Uitz et al. (2008), such that

$$P^B_{m,i} = P^{B_s}_{m,i} \exp(-S^P_i \zeta), \tag{13}$$

and

$$\alpha^B_i = \alpha^{B_s}_i \exp(-S^\alpha_i \zeta), \tag{14}$$

where $P^{B_s}_{m,i}$ and $\alpha^{B_s}_i$ are the surface values for $P^B_{m,i}$ and α^B_i respectively, where $\zeta \sim 0$, and S^P_i and S^α_i represent the rate of change in each parameter ($P^{B_s}_{m,i}$ and $\alpha^{B_s}_i$) with ζ (z/Z_p). Equations 13 and 14 were re-fitted to the data from each size fraction (Fig. 7), and model parameters are provided in Table 2. For all size classes, $P^B_{m,i}$ decreases (significant for all size classes, see Table 2) with ζ and $\alpha^{B_s}_i$ increases (though only significantly for small cells, Table 2), consistent with previous literature (Bouman et al., 2000). In agreement with Uitz et al. (2008), there is a general increase in $P^B_{m,i}$ from small to large cells (Fig. 7). The photoadaptation parameter (I_k), computed as $P^B_{m,i}/\alpha^B_i$, is plotted with ζ (z/Z_p) in Fig. 7, and illustrates how each size class adapts to the changing light environment with depth. The influence of size-specific $P^B_{m,i}$ and $\alpha^{B_s}_i$ on photosynthesis-irradiance curves is illustrated in Fig. 8. In general, there is a decrease in production with

ζ for all size classes at higher light levels (>200 μmol m^{-2} s^{-1}), and a small increase in low light (<100 μmol m^{-2} s^{-1}) for small cells. Equations 13 and 14 were used to estimated $P^B_{m,i}$ and α^B_i for input into Eq. 2, using Z_p (estimated from B_s as in Eq. 3) as input, and parameters are provided in Table 2.

2.5. Irradiance (I)

Equation 2 requires depth-dependent variations in total irradiance ($I(z,t)$) as input. Photosynthetically available radiation (PAR) is a standard product produced by space agencies. It represents total available irradiance from 400 to 700 nanometers, that photosynthetic organisms are able to use in the process of photosynthesis, just above the water surface (where $z \sim 0$). This value is typically provided by space agencies in Einstein m^{-2} d^{-1}, representing integrated irradiance over the daylength (D). We start by converting PAR from Einstein m^{-2} d^{-1} into μmol m^{-2} d^{-1}, then we estimated the surface maximum irradiance just above the water surface ($I_m(0+)$) at mid-day according to

$$I_m(0+) = \frac{\mathrm{PAR}/2}{D}\pi, \tag{15}$$

where daylength (D) is computed following section 2.1. Then, to account for the transmission of light at the air-sea water interface, we subtract 2 % (reflected light) from $I_m(0+)$ to get from above to below water ($I_m(0-)$). This number (2 %) is relatively constant for sun-zenith angles from 0 to 40°, typically observed at local noon in the tropics, but increases with sun-zenith angle (e.g. ~6 % at 60°, see Kirk, 1994) and is impacted by wind speed. Having derived $I_m(0-)$, the

values of irradiance $I(0-,t)$ at various time steps (t) during the day at hourly intervals, just below the air-sea interface, were then computed according to

$$I(0-,t) = \frac{I_m(0-)\sin(\frac{\pi t}{D})}{3600}, \tag{16}$$

where the division by 3600 represents conversion into the average light per second (rather than hours as in the units of D) for that hourly interval (t), such that the units of $I(0-,t)$ are $\mu\text{mol}\,\text{m}^{-2}\,\text{s}^{-1}$, consistent with the units of α^B in the production model (see also photosynthesis-irradiance curves illustrated in Fig. 8). For each hour (t), variations in I with depth (z) are modelled according to the Beer-Lambert Law, such that

$$I(z,t) = I(0-,t)\exp[-K(z)z], \tag{17}$$

where K is the diffuse attenuation coefficient for PAR. The value of K is dependent on the optical properties of the water, which can vary with depth (z). To estimate $K(z)$ we first estimate the average value in the euphotic zone (K_{Zp}), according to

$$K_{Zp} = 4.6/Z_p, \tag{18}$$

where Z_p is estimated using Eq. 3. Figure 1b shows good agreement between $4.6/Z_p$ estimated using Eq. 3 and 18 and K_{Zp} measured on AMT 22 and 23 (see section 2.2). Next we consider $K(z) = K_c + K_v(z)$, where K_c refers to a back-

ground value which we assume to be constant with depth and can be attributed to pure sea water, and $K_v(z)$ is dependent on non-water optical properties, which can vary with depth (z). The value of K_c was computed using Eq. 3 and 18, where surface chlorophyll (B_s) was set to 0.01 mg m^{-3}. Next we estimate $K_v(z)$ by subtracting K_c from K_{Zp}, then weighting the result as a linear function of $B(z)$, yielding the following equation for $K(z)$,

$$K(z) = [(K_{Zp} - K_c)(\frac{B(z)}{1/N \sum_{j=1}^{N} Bj})] + K_c, \tag{19}$$

where $1/N \sum_{j=1}^{N} Bj$ represents the average biomass in the chlorophyll profile ($B(z)$), where $B(z)$ is computed using Eq. 5. This approach ensures vertical variations in $K_v(z)$ follows variations in $B(z)$. Having computed $K(z)$, we estimated $I(z, t)$ using Eqs. 15 to 17, and applied it as input to the primary production model (Eq. 2).

2.6. Example of modelled size-fractionated primary production

A detailed example of application of the primary production model (Eq. 2) is shown in Figure 9. For a specific case (Fig. 9a), at a latitude of 20°, longitude of -30°, day of year (DOY) of 150, B_s of 0.08 mg m^{-3}, PAR of 50.0 Einstein m^{-2} d^{-1} and a Z_m of 50 m, we illustrate how the model functions. First Z_p (104 m) is estimated from B_s using Eq. 3 (Fig. 9a). Next the vertical biomass profile $B(z)$ and $K(z)$ profile are estimated from B_s, Z_p and Z_m (Fig. 9b), using Eq. 5, 18 and 19. Using the model of Brewin et al. (2010b), as described in Eq. 6 to 9 and illustrated in Fig. 9c, the biomass profiles of the three size classes are estimated

from $B(z)$ (Fig. 9d). Using PAR and $K(z)$ together with Eq. 15 through to 19, the irradiance field ($I(z,t)$) is modelled over the daylength (D) and with depth (z), as illustrated in Fig. 9e. Figures 9f and 9g show depth variations in α^B and P_m^B of the three size classes computed using Eq. 13 and 14. Figure 9h shows the vertical profile of biomass-normalised production for the three size classes at noon (hour 6), using I and size-specific α^B and P_m^B, and Fig. 9i shows production (P) at noon for the three size classes (multiplying biomass-normalised production (Fig 9h) with biomass (Fig 9d) for each respective size class). Figure 9j shows total production (sum of the three size classes) from hours 1 through to hour 6 of daylength (D), illustrating an increase in production with increasing irradiance (I). For this example, integrating over depth and daylength (using trapezoidal summation), we estimate the production of 139.5 mg C m^{-2} d^{-1} for small cells (<2μm), 64.6 mg C m^{-2} d^{-1} for medium cells (2-10μm) and 27.1 mg C m^{-2} d^{-1} for large cells (>10μm), making a total of 231.2 mg C m^{-2} d^{-1} (Fig. 9a).

2.7. Satellite data and model validation

2.7.1. Satellite data

To run the size-fractionated primary production model using satellite data we require three inputs: satellite estimates of surface chlorophyll concentration (B_s); satellite estimates of photosynthetically available radiation (PAR); and estimates of mixed-layer depth (Z_m). We used estimates of B_s from the Ocean-Colour Climate Change Initiative (OC-CCI, Version 1.0 available at http://www.oceancolour.org/; Sathyendranath and Krasemann, 2014; Müller et al., 2015a,b; Brewin et al., 2015b), an error-characterised time series of merged

ocean-colour products (MODIS-Aqua, SeaWiFS and MERIS). We elected to use OC-CCI products due to the significant increase in ocean-colour coverage gained by merging data from difference platforms (Maritorena et al., 2010; Sathyendranath and Krasemann, 2014); because the three sensors used in the merged products show temporal consistency at seasonal and inter-annual timescales in the Atlantic (Brewin et al., 2014a); and because the validation of OC-CCI data using *in situ* AMT data shows very good performance (Brewin et al., 2016). For further information on OC-CCI processing, extensive documentation can be found on the following website http://www.esa-oceancolour-cci.org/. For estimates of PAR, we used data from the NASA SeaWiFS sensor (1997-2010), at 9km-by-9km resolution, available from the NASA ocean-colour website (http://oceancolor.gsfc.nasa.gov/). For mixed-layer depth we used a monthly mixed layer depth climatology from de Boyer Montégut et al. (2004), available from http://www.ifremer.fr/cerweb/deboyer/mld/home.php. Monthly data on B_s and PAR were downloaded for the year 2007, and used together with the monthly mixed-layer depth data to estimate size-fractionated primary production for each month in 2007. All datasets were re-gridded to 9km-by-9km resolution, prior to running the size-fractionated primary production model at each grid cell.

2.7.2. Satellite validation

For validation of our model, we require *in situ* data on daily integrated size-fractionated primary production, that are independent of the data used to parameterise the model. We made use of an accumulation of daily, integrated size-fractionated primary production data, collected on an number of AMT cruises

between September 1997 and December 2013 using simulated *in situ* method (period where there was concurrent satellite ocean-colour data from SeaWiFS, MERIS and MODIS), and available through the British Oceanographic Data Centre (BODC: see http://www.bodc.ac.uk/). This includes daily integrated size-fractionated primary production data from AMT 5-6 (methods described by Marañón et al., 2001), AMT 12-16 (methods described by Poulton et al., 2006; Tilstone et al., 2009), and AMT 18-23 (methods described by Tilstone et al., Accepted). Note that for AMT 22 and 23, this data were collected pre-dawn, unlike the samples used to estimate photophysiological parameters in the model which were collected at different locations around local noon on each cruise. All data were derived from ^{14}C on-deck incubations at a range of irradiances (typically from 97% to 1% of surface irradiance) and maintained at a temperature close to that *in situ*. At the end of the incubations, samples were sequentially filtered through polycarbonate filters of different pore sizes (e.g. 0.2μm, 2μm, 10μm and 20μm). Filters were exposed for typically 12 hours to concentrated HCl fumes for removal of inorganic ^{14}C. In all cases the radioactivity of each fraction was determined using a liquid scintillation counter. For further information on methods, the reader is referred to Marañón et al. (2001), Poulton et al. (2006), Tilstone et al. (2009) and Tilstone et al. (Accepted), and AMT cruise reports (http://www.bodc.ac.uk/projects/uk/amt/cruise_programme/). In total, 318 estimates of daily integrated size-fractionated primary production for different size classes were available.

For each sample, daily estimates of B_s (OC-CCI) and PAR (SeaWiFS from

1997-2010 and MODIS-Aqua 2011-2013) were extracted from satellite data, using date and latitude and longitude information. Mixed-layer depths were also estimated from monthly climatologies (de Boyer Montégut et al., 2004) re-gridded to 9km-by-9km resolution, by extracting Z_m from the corresponding month of the climatology at the corresponding latitude and longitude. For all data, we used a multi-pixel box (3×3) surrounding each *in situ* data point, to increase the possibility of an *in situ* measurement being available for comparison and to ensure homogeneity and good quality match-ups. Match-ups were only included if there were more than 50% of data in the nine pixels, and if the standard deviation within the nine pixels was less than 0.3 for $\log_{10}$-transformed B_s, 5.0 for PAR and 10.0 for mixed-layer depth. These criteria were set to ensure homogeneity at the location of the match-up, given the vast differences in spatial scales between the *in situ* and satellite data (Bailey and Werdell, 2006). This resulted in 60 match-ups for total primary production, 54 for the >2μm and <2μm size fractions, and 26 match-ups for the 2-10μm and >10μm size fractions.

Using the satellite data and Z_m estimates as input, daily integrated size-fractionated primary production was estimated using Eq. 2, and compared with the *in situ* data. We used a suite of statistical tests to compare the satellite estimates with the *in situ* data, including: the Pearson correlation coefficient (r); the root mean square error (Ψ); the average bias between model and measurement (δ); the centre-pattern (or unbiased) root mean square error (Δ); the slope (S^T) and intercept (J) of a Type-2 regression, where N is the number of samples. The equations used for each of these statistical tests are provided in Section 4.1 of

Brewin et al. (2015b). All statistical tests were performed in $\log_{10}$ space following previous global primary production comparisons (Campbell et al., 2002; Carr et al., 2006; Friedrichs et al., 2009).

2.8. Sensitivity analysis and model uncertainty

Considering the large number of parameters in the model (Table 2) and considering there are three different model inputs (B, I and Z_m), it is important to understand the sensitivity of the model to realistic uncertainties in model input and model parameters. To do this we used a Monte Carlo approach. We first tested the model by varying all parameters simultaneously, this involved:

- Producing realistic distributions of model input (for a given satellite pixel), based on the input value at given satellite pixel and some estimate of uncertainty in that value (e.g. standard deviation). We assumed normal (Gaussian) distributions of model input, so for B, distributions were produced in $\log_{10}$-space, considering B is typically log-normally distributed (Campbell, 1995). For satellite estimates of B, we used a standard deviation of 0.16 (in $\log_{10}$-space) based on a recent satellite validation of B using AMT data (Brewin et al., 2016). For I (satellite PAR) we assumed standard deviation of 7% based on a NASA satellite validation of SeaWiFS PAR (absolute percentage difference, see NASA, 2016), and for Z_m we assumed a 30% error (the median absolute percentage difference between Z_m computed from 74 CTD profiles on AMT22 using the temperature criterion (same as de Boyer Montégut et al., 2004), with that extracted using the de Boyer Montégut et al. (2004) climatology at the corresponding

533 month and closest latitude and longitude). Figure 10 shows an example
534 of model input distributions for a pixel in the South Atlantic Gyre with
535 $B = 0.08\,\mathrm{mg\,m^{-3}}$, $I = 40\,\mathrm{Einstein\,m^{-2}\,d^{-1}}$ and $Z_m = 30\,\mathrm{m}$.

536 • Producing realistic distributions of model parameters, based on the param-
537 eter value and its standard deviation (Table 2) assuming normal distribu-
538 tions (see Fig. 10).

539 • Once the distributions of model input and parameters were produced,
540 Monte Carlo simulations were performed. This involved: (i) running the
541 model by randomly selecting model input and parameters from their distri-
542 butions; and (ii) repeating for a given number of iterations. This produced
543 a distribution of model output (see Fig. 10).

544 • For each distribution of model output, a standard deviation (Δ) was taken
545 as an index of uncertainty (see Fig. 10). The minimum number of it-
546 erations required to produce a stable estimate of Δ, and thus used in the
547 exercise to minimise computational costs, was determined as 200 (see Fig.
548 11). Standard deviations (Δ) on model output (P_1, P_2 and P_3) were com-
549 puted in $\log_{10}$-space, considering the distribution of model outputs (see
550 Fig. 10).

551 This exercise was conducted on a monthly image in the Atlantic Ocean (October
552 2007), to map spatial variations in Δ for each size class and total P. The image
553 input (B, I and Z_m) was rescaled to 1/3°-by-1/3° resolution to reduce computa-
554 tional costs.

In addition to varying all parameters simultaneously, we also tested the sensitivity of total production and that of each size class to individual variations in each input and parameter, by varying each input and parameter individually (200 random Monte Carlo simulations) whilst keeping the remaining values fixed. This was conducted for three scenarios, an oligotrophic case in the South Atlantic Gyre on the 10$^{\text{th}}$ January (latitude = $-20°$, longitude = $-30°$, $B = 0.05\,\text{mg}\,\text{m}^{-3}$, $I = 55$ Einstein $\text{m}^{-2}\,\text{d}^{-1}$ and $Z_m = 30\,\text{m}$), a mesotrophic case in the equatorial Atlantic on the 19$^{\text{th}}$ August (latitude = $0°$, longitude = $-30°$, $B = 0.2\,\text{mg}\,\text{m}^{-3}$, $I = 40$ Einstein $\text{m}^{-2}\,\text{d}^{-1}$ and $Z_m = 50\,\text{m}$), and a well-mixed eutrophic case in the North Atlantic on the 10$^{\text{th}}$ April (latitude = $45°$, longitude = $-30°$, $B = 2.0\,\text{mg}\,\text{m}^{-3}$, $I = 10$ Einstein $\text{m}^{-2}\,\text{d}^{-1}$ and $Z_m = 100\,\text{m}$).

3. Results and Discussion

3.1. Validation results

In general, the satellite model, using parameters from Table 2, performs well when compared with *in situ* data (Fig. 12), with correlation coefficients (r) ranging from 0.68 to 0.85, and root mean square errors (Ψ) from 0.23 to 0.32, for the size classes and total production. These statistics are comparable to studies that have tested satellite models of total primary production using *in situ* data, for instance: Campbell et al. (2002) shows Ψ ranging from 0.28 to 0.51 for 12 satellite models; Friedrichs et al. (2009) shows Ψ ranging from 0.23 to 0.39 for 21 satellite models; and Tilstone et al. (2009) shows Ψ ranging from 0.22 to 0.29, and r from 0.69 to 0.77, for three different satellite models. Biases (δ)

range from −0.12 to 0.01 (Fig. 12), indicating no major systematic differences between the satellite model estimates and *in situ* data (Fig. 12). However, for the smaller size classes (<2μm and 2-10μm), the satellite model seems to underestimate production at higher rates and overestimate slightly at lower rates, as emphasised by slopes (S_T) of 0.33 and 0.44 for the two smaller size classes (<2μm and 2-10μm).

The majority of data points in the validation lie within ±30% production in $\log_{10}$ space (Fig. 12 dashed lines). Considering: (i) to our knowledge, this is the first independent evaluation of satellite-based, size-fractionated primary production estimates over the entire Atlantic Ocean; (ii) that statistical tests compare well with studies that have compared satellite models of total primary production model with *in situ* data; (iii) the potential differences arising from mismatch in spatial scales between satellite and *in situ* data; (iv) variability in the methods used to determine *in situ* size-fractionated production on the different AMT cruises; and (v) potential biases associated with comparing production model outputs with ^{14}C daily incubations; results from the validation (Fig. 12) are encouraging and give confidence in the application of the proposed model to satellite data.

3.2. Application to satellite data

Figure 13 show total production (P) and size-fractionated production (P_i) for two months in 2007, May and October (typical months where AMT cruises have occurred). The seasonal patterns in total production (P) are consistent with previous studies (Platt and Sathyendranath, 1991; Longhurst et al., 1995; Sathyen-

600 dranath et al., 1995; Antoine et al., 1996; Behrenfeld and Falkowski, 1997; Uitz
601 et al., 2010). Production is greater at high latitudes during the spring (May for
602 the northern hemisphere and October for the southern hemisphere) and lower at
603 high latitudes during months closer to the winter solstice (October for the north-
604 ern hemisphere and May for the southern hemisphere in Fig 13). Lowest pro-
605 duction is found in the oligotrophic gyres, increasing in equatorial regions, and
606 highest in coastal areas, upwelling regions and at high latitudes during spring.

607 Large cells (P_3) dominate production in the sub-Arctic and sub-Antarctic
608 during spring, in upwelling zones and in coastal regions. Elsewhere, P_3 is
609 low, particularly in the oligotrophic gyres. Similar to large cells, both medium
610 cells (P_2) and small cells (P_1) have higher production rates in eutrophic and
611 mesotrophic regions. However, they contribute more to production offshore of
612 the coastal upwelling zones, and in the equatorial Atlantic. Small cells (P_1) have
613 the highest production rates in the oligotrophic gyres (Fig 13).

614 Figure 14 shows the fraction of total integrated chlorophyll biomass and total
615 primary production for each size class in the Atlantic Ocean for October 2007.
616 In both cases, small cells contribute the highest to biomass and production over
617 most of the Atlantic Ocean, particularly in the oligotrophic gyres, but only a
618 small fraction in upwelling zones, coastal regions and during the spring bloom.
619 The contribution of medium cells (P_2) to both biomass and production is con-
620 stant over the majority of the Atlantic (Fig. 14), but decreases in coastal regions
621 associated with very high production (Fig 13). Large cells are shown to dominate
622 at very high biomass and production, elsewhere their contribution to chlorophyll

biomass and production is low.

Figure 14 illustrates that the contribution of large and medium (small) cells is slightly higher (lower) for production when compared with chlorophyll biomass, reflecting that normalised production increases with size class in the model (Fig. 8). These results are consistent with previous studies on AMT. Marañón et al. (2001) observed that small cells (<2μm) account for an average of 56% of the total primary production and 71% of the chlorophyll on an Atlantic Meridional Transect, with this contribution highest in oligotrophic waters and decreasing in temperate waters. Higher chlorophyll-normalised production rates for medium and large cells (2-10μm and >10μm) in the model (Fig. 8) are consistent with previous studies in the Atlantic (Fernández et al., 2003; Claustre et al., 2005; Poulton et al., 2006) and in some coastal eutrophic systems (Cermeño et al., 2005a,b), but are at odds with allometric scaling relationships that show a general inverse relationship between phytoplankton size and growth rates (Chisholm, 1992), and disagree with some studies that suggest environments dominated by small cells are characterised by high photosynthetic rates (Laws et al., 1987; Bouman et al., 2005). Other studies have suggested a unimodal relationship between phytoplankton cell size and biomass-specific metabolic rate (Raven, 1994; Marañón et al., 2013; Marañón, 2015), which is consistent with an increase in photosynthetic rates from small (<2μm) to medium (2-10μm) sized cells, but not with an increase from medium (2-10μm) to large (>10μm) cells. However, the relationship between maximum realised growth rate and assimilation number depends on the carbon-to-chlorophyll ratio, which can vary with light and com-

munity structure. It could be that our results reconcile with those of Marañón et al. (2013) when considering variations in carbon-to-chlorophyll. The large variability in $P^B_{m,i}$ and α^B (Fig. 7) for all size classes suggest further work is required to understand variability in size-fractionated photosynthetic rates.

Figure 15 shows 2D histograms of size-fractionated primary production plotted as a function of total primary production (top row), and the fractions of each size class to total primary production plotted as a function of the total primary production (bottom row). Data in Fig 15 are from monthly Atlantic satellite images for 2007, run using the size-fractionated primary production model. The model output highlights general relationships between size-fractionated production and total, with large cells (>10μm) contributing at high total production (P) and smaller cells (<10μm, 2-10μm and <2μm) at lower production. However, there is significant variability surrounding these general patterns. For instance, at 200 mgC m^{-2} d^{-1} of total production, the fraction of large cells (P_3/P) can vary from 0.1 to 0.8. The figure also emphasises that the model constrains primary production of small and medium cells (<10μm) to values lower than 700 mgC m^{-2} d^{-1}.

The important role of phytoplankton size in biogeochemical processes has been well documented in recent years (Marañón, 2009, 2015; Finkel et al., 2010; Brewin et al., 2014c; IOCCG, 2014). Large cells (>10μm) contribute a considerable amount to new (nitrate-based) primary production and carbon export (Eppley and Peterson, 1979; Michaels and Silver, 1988; Silió-Calzada et al., 2008; Uitz et al., 2010; Briggs et al., 2011; Tilstone et al., Accepted). Figure

669 16 illustrates monthly images of primary production by large cells, and indi-
670 rectly, expected seasonality in new primary production and carbon export. High
671 rates of primary production from large cells are observed in spring periods in
672 each hemisphere and in upwelling regions such as the Benguela (Hirata et al.,
673 2009). Output from size-fractionated primary production models, such as that
674 illustrated in Fig. 16, has applications for multi-phytoplankton biogeochemical
675 model evaluation (Ward et al., 2012; Hirata et al., 2013; de Mora et al., 2016),
676 and may even be useful in a data assimilation scheme, to improve simulations of
677 biogeochemical rates (Xiao and Friedrichs, 2014).

678 *3.3. Model sensitivity and uncertainty results*

679 For October 2007, spatial variations in Δ derived from the Monte Carlo sim-
680 ulations for total production and production in each size class are shown in Fig.
681 17. For most products, Δ is higher in the oligotrophic gyres and decreases in
682 meso- and eutrophic waters (e.g. high latitude regions, upwelling zones and
683 equatorial regions). In general, Δ is lower for total production (P) and produc-
684 tion for small cells (P_1), with average values of 0.27 and 0.26 respectively. These
685 values compare well with Δ from the validation exercise (of 0.23 for P and 0.25
686 for P_1, see Fig. 12). Consistent with the validation (Fig. 12), Δ from the Monte
687 Carlo simulations is higher for P_2 and P_3. However, the average values of Δ for
688 P_2 and P_3 (0.63 and 0.43 respectively, see Fig. 17) are significantly higher than
689 those from the validation (0.29 and 0.30 respectively). It is important to note that
690 results from these Monte Carlo simulations make two assumptions which may
691 not always hold: i) normality in the parameter and input distributions; and ii) that

692 the uncertainties in model input and parameters are random (i.e. not correlated).

693 The sensitivity of the model (Δ) to individual variations in model input and
694 parameters, for three different cases (oligotrophic, mesotrophic and eutrophic)
695 and for total production and that of the different size classes, is plotted in Fig.
696 18. For the three inputs (B, I and Z_m), variations in B seem the most sensitive,
697 which is not surprising considering many of the parameters are tied to B, and
698 that B plays such a prominent role in the estimation of production. In the olig-
699 otrophic case (Fig. 18a) and eutrophic case (Fig. 18c) variations in I appear
700 more sensitive than Z_m, though in the mesotrophic case (Fig. 18b) Z_m is more
701 sensitive, likely due to variations in Z_p/Z_m osculating between 1.0 and 1.5 during
702 this Monte Carlo simulation and impacting estimates of the vertical profile of B
703 (see Fig. 3c and Fig. 4).

704 Regarding the model parameters, is it clear in all cases the importance of
705 computing Z_p accurately, as indexed by the sensitivity of parameters q_a and q_b
706 (Fig. 18). For stratified conditions (Fig. 18a and b), of the parameters that control
707 the vertical profile of B, the background slope (S^{Bs}) and the width of the peak
708 (σ) appear the most sensitive, impacting all production estimates. In general,
709 the assimilation number and initial slopes (P_m^B and α^B) are less sensitive than
710 other model parameters, but size-specific variations in these parameters clearly
711 impact production in the corresponding size class (Fig. 18). Though they have
712 a relatively small impact on estimates of total production (P) and to some extent
713 small cells (P_1), P_2 and P_3 are very sensitive to the parameters controlling the
714 partitioning of total chlorophyll into the three size classes ($B_{1,2}^m$, B_1^m, $S_{1,2}$ and

S_1). From this analysis (Fig. 18), we can deduce that higher values of Δ in Fig. 17 for P_2 and P_3 are likely related to uncertainty in these parameters. This is particularly true for the high Δ values for P_2 (Fig. 17), considering unlike P_1 and P_3, all four parameters ($B^m_{1,2}$, B^m_1, $S_{1,2}$ and S_1) are required to estimate P_2. The sensitivity analysis is very useful for targeting key parameters where future AMT monitoring efforts could focus to help reduce model uncertainties.

3.4. Comparison with the model of Uitz et al. (2010) in the Atlantic.

Uitz et al. (2010) provide annual estimates of total and size-fractionated primary production in the Atlantic Ocean, using their satellite model (Uitz et al., 2006, 2008), which are compared with estimates from our model (Table 3). For 2007, we estimated 7.9 Gt C y^{-1} of total primary production, which is lower than climatological estimates (12.2 Gt C y^{-1}) from Uitz et al. (2010). Differences between these two approaches are most striking in the percentage contribution of small cells (<2μm) and the sum of medium and large cells (>2μm) to total production (Table 3). In the Uitz et al. (2010) study, small cells contribute ~20 % to total production in the Atlantic, whereas our estimates are closer to 50 %.

Differences in photosynthetic parameters ($P^B_{m,i}$ and α^B_i) between Uitz et al. (2008) and our model may partly explain these differences, especially when considering higher P^B_m values in our model for small cells (Fig. 7). However, it is likely that the main cause can be traced back to differences in the contribution of small cells to total chlorophyll biomass (B_1/B) between the two approaches. In our model, B_1/B is 0.6 to 0.7 over the majority of the Atlantic (Fig. 14), whereas in the Uitz et al. (2008) model (see Fig. 13c of Uitz et al., 2006), B_1/B is typi-

cally 0.2 to 0.5. This disparity arises from systematic differences between size-fractionated chlorophyll derived using the sequential filtration technique (used here), and inferred from HPLC data (as conducted by Uitz et al., 2006, 2008). To derive size-fractionated chlorophyll from measurements of total HPLC requires attributing specific diagnostic pigments to each of the three size classes, for instance, fucoxanthin with microplankton and zeaxanthin with picoplankton (Uitz et al., 2006). However, concentrations of these diagnostic pigments have been observed in all size classes (Uitz et al., 2009) and taxonomic groups harbouring specific diagnostic pigments can vary in size. Whereas sequential size-fractionated filtration explicitly partitions the size classes, the technique also has caveats, and uncertainties can arise from inaccuracies in pore sizes, filter clogging (e.g. from chain-forming species) and phytoplankton cell breakage.

Brewin et al. (2014b) used concurrent data on size-fractionated chlorophyll estimated by these two methods and found HPLC estimates of chlorophyll in small cells (<2μm) were consistently lower when using the HPLC method. The impact on model parameters when fitting a three-component model (Eqs. 7, B_1^m and S_1) to these two separate datasets (HPLC and sequential size-fractionated filtration) was shown by Brewin et al. (2014c), with significantly higher values of B_1^m and lower values of S_1 when using sequential size-fractionated filtration data compared with the HPLC method (see Table 2 and Fig. 2 of Brewin et al., 2014c). Uncertainty in the two approaches makes it difficult to ascertain which provides more reliable estimates (Brewin et al., 2014b). Future work, perhaps incorporating other sources of *in situ* data (e.g. flow cytometry and microscopy),

761 is required to help understand the differences in size-fractionated chlorophyll
762 between the two techniques.

763 *3.5. Routes to future improvements in estimating size-fractionated primary pro-*
764 *duction*

765 Our approach to modelling size-fractionated primary production is based on
766 an established and proven primary production model (Platt et al., 1980). When
767 applied to satellite data, our model has been shown to perform well when com-
768 pared with independent *in situ* measurements (Fig. 12), and reproduces expected
769 seasonal cycles in total and size-fractionated primary production (Figs. 13 and
770 16). Yet further improvements to the approach could be investigated in future
771 studies.

772 For the smaller size classes (<2μm), the satellite model underestimates pro-
773 duction at higher rates and overestimates slightly at lower rates when compared
774 with *in situ* data (Fig. 12). The filtration method used here is likely to capture the
775 bulk photosynthetic rates for picoplankton (<2μm) but unlikely to capture vari-
776 ability among taxonomic communities with this size class. The photophysiolog-
777 ical rates of the three dominant picoplankton groups in the Atlantic (*Prochloro-*
778 *coccus*, *Synechococcus*, and picoeukaryotes) differ from each other (Veldhuis
779 et al., 2005). There is evidence that *in situ* growth rates of *Synechococcus* ex-
780 ceed those of *Prochlorococcus* (Furnas and Crosbie, 1999), and *Prochlorococcus*
781 are more dominant within the oligotrophic gyres, with higher concentrations of
782 *Synechococcus* in temperate waters (Zubkov et al., 2000). Shifts in the taxo-
783 nomic community within the picoplankton size class, and hence photosynthetic

rates, from low production (gyre, *Prochlorococcus* dominated) waters to higher production (temperate, *Synechococcus* dominated) waters (Bouman et al., 2011; Mouriño Carballido et al., 2016), may explain biases observed in Fig. 12. Future efforts could be made to incorporate such taxonomic variations into the model (e.g. Hirata et al., 2011).

We used a broadband model (Eq. 2) to estimate size-fractionated primary production which does not resolve spectral variations in light. In some cases, this can result in biases in production (Kyewalyanga et al., 1992; Lorenzo et al., 2004), and may be important when modelling different size classes, considering that the shape of the phytoplankton absorption spectrum changes with size (Sathyendranath et al., 2004; Devred et al., 2006; Uitz et al., 2010; Brewin et al., 2011). Future efforts could be made to convert Eq. 2 into a spectral model, such that spectral variations in I and α^B_i were admitted in the calculations.

Our approach (Eq. 2) does not account for diurnal variations in chlorophyll (B) or photosynthetic rates ($P^B_{m,i}$ and α^B_i), despite evidence that such variations occur in nature (Yentch and Ryther, 1957; Harding et al., 1981; Rivkin and Putt, 1987; Bruyant et al., 2005). In future studies, it may be possible to incorporate information from geostationary ocean-colour observations (e.g. GOCI; Choi et al., 2012) together with techniques to extract physiological information from diurnal cycles in optical proxies (e.g. Dall'Olmo et al., 2011), to account for diurnal variations in B, $P^B_{m,i}$ and α^B_i.

Whereas our approach models diurnal variations in broadband irradiance, and accounts for vertical variations in K, further improvements to the light field

could be made, for instance: (i) incorporating diurnal variations in K caused by diurnal variations in water constituents (e.g. chlorophyll) and sun-zenith angle; (ii) accounting for variations between chlorophyll and other water constituents (e.g. coloured dissolved matter) with depth that may impact K; (iii) incorporating the influence of diurnal variations in cloud cover on irradiance, using information from geostationary observations; (iv) incorporating variations in sun-zenith angle and wind speed on the transmission of light at the air-sea water interface (Kirk, 1994); (v) incorporating spectral variability in irradiance with depth (Sathyendranath and Platt, 1988, 2007); and (vi) improving estimates of I_m (Eq.15) from daily PAR at high latitudes. In all cases, increased model complexity needs to be justified by improved model performance (law of parsimony).

The parameters of the model are based on data collected on AMT at a specific time of year (September-November), and therefore, not likely to capture seasonal variations in photosynthetic rates (e.g. Platt and Sathyendranath, 1991). The model assumes both the size structure and vertical changes in B covary with surface chlorophyll (Uitz et al., 2006), when seasonal variations in these relationships may occur (Platt and Sathyendranath, 1991; Sathyendranath et al., 1995; Devred et al., 2006). In fact, many of the model parameters (Z_p, B_i, $P^B_{m,i}$, α^B_i and K) are directly or indirectly tied to surface chlorophyll in our model. Incorporating other environmental data (e.g. SST, PAR, wind) to capture variations surrounding these general relationships may improve model performance (Saux Picart et al., 2014; Brewin et al., 2015a; Ward, 2015). In recent years, there has been a global increase in the number of Argo and Bio-Argo floats deployed

to capture seasonal variations in the vertical structure of chlorophyll biomass (Xing et al., 2011; Mignot et al., 2014), size structure (Sauzède et al., 2015) and mixed-layer depth (Johnson et al., 2012). In the future, there is potential to integrate observations from Argo floats with satellite data to improve global estimates of size-fractionated primary production.

4. Summary

We re-tuned a remote-sensing technique to estimate primary production in three phytoplankton size classes (<2μm, 2-10μm and >10μm) in the Atlantic Ocean. We parameterised the model using measurements of total chlorophyll biomass, euphotic depth, size-fractionated chlorophyll biomass and size-fractionated photosynthesis-irradiance experiments, collected on AMT cruises. The performance of the remote-sensing technique was evaluated with independent estimates of size-fractionated primary production collected on a number of AMT cruises using ^{14}C incubation experiences, and gave confidence in the application of the model to satellite data. Monte Carlo simulations, incorporating uncertainty in the satellite inputs and model parameters, suggest an average model error of between 0.27 and 0.63 for $\log_{10}$-transformed size-fractionated production, with errors generally higher in oligotrophic waters and higher for the larger size classes (2-10μm and >10μm). We applied the model to monthly satellite data in 2007, and results suggest cells <2μm and >2μm contribute equally to total primary production in the Atlantic Ocean.

5. Acknowledgments

The authors would like to thank the Ocean Biology Processing Group of NASA for the processing and distribution of the SeaWiFS data, and the European Space Agency (ESA) for the distribution of OC-CCI data. We sincerely thank officers and crew of the RRS James Clark Ross, RRS James Cook and RRS Discovery, for their help during the AMT cruises and all those involved in data collection and analysis. This work is supported by the UK National Centre for Earth Observation. AMT data were supported by the UK Natural Environment Research Council National Capability funding to Plymouth Marine Laboratory and the National Oceanography Centre, Southampton. This is a contribution to the Ocean Colour Climate Change Initiative of ESA, and contribution number xxx of the AMT programme. This work was supported by an internal Research Project funded by Plymouth Marine Laboratory. We thank Trevor Platt, Shubha Sathyendranath, the editors and two anonymous reviewers for valuable comments on our manuscript.

References

Aiken, J., Pradhan, Y., Barlow, R., Lavender, S., Poulton, A., Holligan, P., Hardman-Mountford, N. J., 2009. Phytoplankton pigments and functional types in the Atlantic Ocean: A decadal assessment, 1995-2005. Deep Sea Research I 56 (15), 899–917.

Aiken, J., Rees, N., Hooker, S., Holligan, P., Bale, A., Robins, D., Moore, G.,

873 Harris, R., Pilgrim, D., 2000. The Atlantic Meridional Transect: overview and
874 synthesis of data. Progress in Oceanography 45, 257–312.
875 Airs, R., Martinez-Vicente, V., 2014a. AMT18 (JR20081003) HPLC pigment
876 measurements from CTD bottle samples. British Oceanographic Data Centre
877 - Natural Environment Research Council, UK. doi:10/tk2.
878 Airs, R., Martinez-Vicente, V., 2014b. AMT19 (JR20081003) HPLC pigment
879 measurements from CTD bottle samples. British Oceanographic Data Centre
880 - Natural Environment Research Council, UK. doi:10/tk3.
881 Airs, R., Martinez-Vicente, V., 2014c. AMT20 (JR20081003) HPLC pigment
882 measurements from CTD bottle samples. British Oceanographic Data Centre
883 - Natural Environment Research Council, UK. doi:10/tk4.
884 Antoine, D., André, J.-M., Morel, A., 1996. Ocean primary production 2 Esti-
885 mation at global scale from satellite (coastal zone color scanner) chlorophyll.
886 Global Biogeochemical Cycles 10, 57–69.
887 Aumont, O., Maier-Reimer, E., Blain, S., Monfray, P., 2003. An ecosystem
888 model of the global ocean including Fe, Si, P colimitations. Global Biogeo-
889 chemical Cycles 17 (2), 1060.
890 Bailey, S. W., Werdell, P. J., 2006. A multi-sensor approach for the on-orbit
891 validation of ocean color satellite data products. Remote Sensing Environment
892 102, 12–23.
893 Behrenfeld, M., Falkowski, P., 1997. Photosynthetic rates derived from satellite-
894 based chlorophyll concentration. Limnology and Oceanography 42, 1–20.
895 Blackford, J. C., Allen, J. I., Gilbert, F. J., 2004. Ecosystem dynamics at six

896 contrasting sites: a generic modelling study. Journal of Marine Systems 52 (1-
897 4), 191–215.
898 Bouman, H., Platt, T., Kraay, G. W., Sathyendranath, S., Irwin, B. D., 2000.
899 Bio-optical properties of the subtropical North Atlantic. I. Vertical variability.
900 Marine Ecological Progress Series 200, 3–18.
901 Bouman, H., Platt, T., Sathyendranath, S., Stuart, V., 2005. Dependence of light-
902 saturated photosynthesis on temperature and community structure. Deep-Sea
903 Research I 52, 1284–1299.
904 Bouman, H. A., Ulloa, O., Barlow, R., Li, W. K., Platt, T., Zwirglmaier, K., Scan-
905 lan, D. J., Sathyendranath, S., 2011. Water-column stratification governs the
906 community structure of subtropical marine picophytoplankton. Environmental
907 Microbiology Reports 3, 473–482.
908 Brewin, R. J. W., Dall'Olmo, G., Pardo, S., van Dongen-Vogel, V., Boss, E. S.,
909 2016. Underway spectrophotometry along the Atlantic Meridional Transect
910 reveals high performance in satellite chlorophyll retrievals. Remote Sensing
911 of Environment 183, 82–97.
912 Brewin, R. J. W., Devred, E., Sathyendranath, S., Hardman-Mountford, N. J.,
913 Lavender, S. J., 2011. Model of phytoplankton absorption based on three size
914 classes. Applied Optics 50 (2), 4535–4549.
915 Brewin, R. J. W., Lavender, S. J., Hardman-Mountford, N. J., 2010a. Mapping
916 size-specific phytoplankton primary production on a global scale. Journal of
917 Maps, 448–462.
918 Brewin, R. J. W., Mélin, F., Sathyendranath, S., Steinmetz, F., Chuprin, A.,

919 Grant, M., 2014a. On the temporal consistency of chlorophyll products de-
920 rived from three ocean-colour sensors. ISPRS Journal of Photogrammetry and
921 Remote Sensing 97, 171–184.
922 Brewin, R. J. W., Sathyendranath, S., Hirata, T., Lavender, S. J., Barciela, R.,
923 Hardman-Mountford, N. J., 2010b. A three-component model of phytoplank-
924 ton size class for the Atlantic Ocean. Ecological Modelling 221, 1472–1483.
925 Brewin, R. J. W., Sathyendranath, S., Jackson, T., Barlow, R., Brotas, V., Airs,
926 R., Lamont, T., 2015a. Influence of light in the mixed layer on the parameters
927 of a three-component model of phytoplankton size structure. Remote Sensing
928 of Environment 168, 437–450.
929 Brewin, R. J. W., Sathyendranath, S., Lange, P. K., Tilstone, G., 2014b. Com-
930 parison of two methods to derive the size-structure of natural populations of
931 phytoplankton. Deep Sea Research I 85, 72–79.
932 Brewin, R. J. W., Sathyendranath, S., Müller, D., Brockmann, C., Deschamps, P.-
933 Y., Devred, E., Doerffer, R., Fomferra, N., Franz, B. A., Grant, M., Groom, S.,
934 Horseman, A., Hu, C., Krasemann, H., Lee, Z.-P., Maritorena, S., Mélin, F.,
935 Peters, M., Platt, T., Regner, P., Smyth, T., Steinmetz, F., Swinton, J., Werdell,
936 J., White III, G. N., 2015b. The Ocean Colour Climate Change Initiative: III.
937 A round-robin comparison on in-water bio-optical algorithms. Remote Sens-
938 ing Environment 162, 271–294.
939 Brewin, R. J. W., Sathyendranath, S., Tilstone, G., Lange, P. K., Platt, T., 2014c.
940 A multicomponent model of phytoplankton size structure. Journal of Geo-
941 physical Research 119, 3478–3496.

Briggs, N., Perry, M. J. P., Cetinić, I., Lee, C., D'Asaro, E., Gray, A. M., Rehm, E., 2011. High-resolution observations of aggregate flux during a sub-polar North Atlantic spring bloom. Deep Sea Research I 58, 1031–1039.

Bruyant, F., Babin, M., Genty, B., Prasil, O., Behrenfeld, M., Claustre, H., Bricaud, A., Garczarek, L., Holtzendorff, J., Koblizek, M., Dousova, H., Partensky, F., 2005. Diel variations in the photosynthetic parameters of *Prochlorococcus* strain PCC 9511: Combined effects of light and cell cycle. Limnology and Oceanography 50, 850–863.

Campbell, J. W., 1995. The lognormal distribution as a model for bio-optical variability in the sea. Journal of Geophysical Research 100(C7), 13237–13254.

Campbell, J. W., Antoine, D., Armstrong, R. A., Arrigo, K. R., Balch, W., Barber, R., Behrenfeld, M., Bidigare, R., Bishop, J., Carr, M.-E., Esaias, W., Falkowski, P., Hoepffner, N., Iverson, R., Kiefer, D. A., Lohrenz, S., Marra, J., Morel, A., Ryan, J., Vedernikov, V., Waters, K., Yentch, C., Yoder, J., 2002. Comparison of algorithms for estimating ocean primary production from surface chlorophyll, temperature, and irradiance. Global Biogeochemical Cycles 16, 1035.

Carr, M. E., Friedrichs, M. A., Schmeltz, M., Aita, M. N., Antoine, D., Arrigo, K. R., Asanuma, I., Aumont, O., Barber, R., Behrenfeld, M., Bidigare, R., Buitenhuis, E. T., Campbell, J. W., Ciotti, A. M., Dierssen, H. M., Dowell, M., Dunne, J., Esaias, W., Gentili, B., Gregg, W. W., Groom, S., Hoepffner, N., Ishizaka, J., Kameda, T., Le Quéré, C., Lohrenz, S., Marra, J., Mélin, F.,

965 Moore, K., Morel, A., Reddy, T. E., Ryan, J., Scardi, M., Smyth, T., Turpie,
966 K., Tilstone, G., Waters, K., Yamanaka, Y., 2006. A comparison of global
967 estimates of marine primary production from ocean color. Deep Sea Research
968 Part II: Topical Studies in Oceanography 53, 741–770.
969 Cermeño, P., Estévez-Blanco, P., Marañón, E., Fernández, E., 2005a. Maximum
970 photosynthetic efficiency of size-fractionated phytoplankton assessed by ^{14}C
971 uptake and fast repetition rate fluorometry. Limnology and Oceanography 50,
972 1438–1446.
973 Cermeño, P., Marañón, E., Rodríguez, J., Fernández, E., 2005b. Large-sized
974 phytoplankton sustain higher carbon-specific photosynthesis than smaller cells
975 in a coastal eutrophic ecosystem. Marine Ecological Progress Series 297, 51–
976 60.
977 Chassot, E., Bonhommeau, S., Dulvy, N. K., Mélin, F., Watson, R., Gascuel,
978 D., Le Pape, O., 2010. Global marine primary production constrains fisheries
979 catches. Ecology Letters 13, 495–505.
980 Chisholm, S. W., 1992. Phytoplankton size. In: Falkowski, P. G., Woodhead,
981 A. D. (Eds.), Primary Productivity and Biogeochemical Cycles in the Sea.
982 Springer, New York, pp. 213–237.
983 Choi, J.-K., Park, Y. J., Ahn, J. H., Lim, H.-S., Eom, J., Ryu, J.-H., 2012. GOCI,
984 the world's first geostationary ocean color observation satellite, for the moni-
985 toring of temporal variability in coastal water turbidity. Journal of Geophysical
986 Research 117, C09004.
987 Claustre, H., Babin, M., Merien, D., Ras, J., Prieur, L., Dallot, S., Prasil, O.,

988 Dousova, H., Moutin, T., 2005. Towards a taxon-specific parameterization of
989 bio-optical models of primary production: A case study in the North Atlantic.
990 Journal of Geophysical Research 110, C07S12.
991 Dall'Olmo, G., Boss, E., Behrenfeld, M., Westberry, T. K., Courties, C., Prieur,
992 L., Pujo-Pay, M., Hardman-Mountford, N. J., Moutin, T., 2011. Inferring phy-
993 toplankton carbon and eco-physiological rates from diel cycles of spectral par-
994 ticulate beam-attenuation coefficient. Biogeosciences 8, 3423–3439.
995 de Boyer Montégut, C., Madec, G., Fisher, A. S., Lazar, A., Iudicone, D., 2004.
996 Mixed layer depth over the global ocean: An examination of profile data and
997 a profile-based climatology. Journal of Geophysical Research 109, C12003.
998 de Mora, L., Butenschön, M., Allen, J. I., 2016. The assessment of a global
999 marine ecosystem model on the basis of emergent properties and ecosystem
1000 function: a case study with ERSEM. Geoscience Model Development 9, 59–
1001 76.
1002 Devred, E., Sathyendranath, S., Stuart, V., Maas, H., Ulloa, O., Platt, T., 2006. A
1003 two-component model of phytoplankton absorption in the open ocean: Theory
1004 and applications. Journal of Geophysical Research 111, C03011.
1005 Eppley, R. W., 1972. Temperature and phytoplankton growth in the sea. Fishery
1006 Bulletin 70, 1063–1085.
1007 Eppley, R. W., Peterson, B. J., 1979. Particulate organic matter flux and plank-
1008 tonic new production in the deep ocean. Nature 282, 677–680.
1009 Fernández, E., Marañón, E., Morán, X. A. G., Serret, P., 2003. Potential causes
1010 for the unequal contribution of picophytoplankton to total biomass and pro-

1011 ductivity in oligotrophic waters. Marine Ecological Progress Series 254, 101–
1012 109.
1013 Field, C. B., Behrenfeld, M. J., Randerson, J. T., Falkowski, P. G., 1998. Primary
1014 production of the biosphere: integrating terrestrial and oceanic components.
1015 Science 281, 237–240.
1016 Finkel, Z. V., Beardall, J., Flynn, K., Quigg, A., Rees, T. A. V., Raven, J. A.,
1017 2010. Phytoplankton in a changing world: cell size and elemental stoichiom-
1018 etry. Journal of Plankton Research 32 (1), 119–137.
1019 Forsythe, W. C., Rykiel Jr, E. J., Stahl, R. S., Wu, H., Schoolfield, R. M., 1995.
1020 A model comparison for daylength as a function of latitude and day of year.
1021 Ecological Modelling 80, 87–95.
1022 Friedrichs, M. A. M., Carr, M.-E., Barber, R. T., Scardi, M., Antoine, D., Arm-
1023 strong, R. A., Asanuma, I., Behrenfeld, M., Buitenhuis, E. T., Chai, F., Chris-
1024 tian, J. R., Ciotti, A. M., Doney, S. C., Dowell, M., Dunne, J., Gentili, B.,
1025 Gregg, W. W., Hoepffner, N., Ishizaka, J., Kameda, T., Lima, I., Marra, J.,
1026 Mélin, F., Moore, J. K., Morel, A., O'Malley, R. T. O., O'Reilly, J. E., Saba,
1027 V. S., Schmeltz, M., Smyth, T. J., Tjiputraw, J., Waters, K., Westberry, T. K.,
1028 Winguth, A., 2009. Assessing the uncertainties of model estimates of primary
1029 productivity in the tropical Pacific Ocean. Journal of Marine Systems 76 (1-2),
1030 113–133.
1031 Furnas, M., Crosbie, N., 1999. In situ growth dynamics of the photosynthetic
1032 prokaryotic picoplankters *Synechococcus* and *Prochlorococcus*. In: Charpy,
1033 L., Larkum, A. (Eds.), Marine Cyanobacteria. Vol. 19. Bull. Inst. Océanogr.

1034 Monaco, numéro spécial, pp. 387–417.
1035 Guidi, L., Stemmann, L., Jackson, G. A., Ibanez, F., Claustre, H., Legendre,
1036 L., Picheral, M., Gorskya, G., 2009. Effects of phytoplankton community on
1037 production, size and export of large aggregates: A world-ocean analysis. Lim-
1038 nology and Oceanography 54 (6), 1951–1963.
1039 Harding, L. W. J., Meeson, B. B., Prézelin, B. B., Sweeney, B. M., 1981. Diel
1040 periodicity of photosynthesis in marine phytoplankton. Marine Biology 61,
1041 95–105.
1042 Hirata, T., Hardman-Mountford, N. J., Barlow, R., Lamont, T., Brewin, R. J. W.,
1043 Smyth, T., Aiken, J., 2009. An inherent optical property approach to the es-
1044 timation of size-specific photosynthetic rates in eastern boundary upwelling
1045 zones from satellite ocean colour: an initial assessment. Progress in Oceanog-
1046 raphy 83, 393–397.
1047 Hirata, T., Hardman-Mountford, N. J., Brewin, R. J. W., Aiken, J., Barlow, R.,
1048 Suzuki, K., Isada, T., Howell, E., Hashioka, T., Noguchi-Aita, M., Yamanaka,
1049 Y., 2011. Synoptic relationships between surface chlorophyll-a and diagnostic
1050 pigments specific to phytoplankton functional types. Biogeosciences 8, 311–
1051 327.
1052 Hirata, T., Saux Picart, S., Hashioka, T., Aita-Noguchi, M., Sumata, H.,
1053 Shigemitsu, M., Allen, J. I., Yamanaka, Y., 2013. A comparison between phy-
1054 toplankton community structures derived from a global 3D ecosystem model
1055 and satellite observation. Journal of Marine Systems 109-101, 129–137.
1056 IOCCG, 2014. Phytoplankton Functional Types from Space. Tech. rep., Sathyen-

dranath, S. (e.d.), Reports of the International Ocean-Colour Coordinating Group, No. 15, IOCCG, Dartmouth, Canada.

Johnson, G. C., Schmidtko, S., Lyman, J. M., 2012. Relative contributions of temperature and salinity to seasonal mixed layer density changes and horizontal density gradients. Journal of Geophysical Research 117, C04015.

Kirk, J. T. O., 1994. Light and photosynthesis in Aquatic Ecosystems. Cambridge Univeristy Press.

Kishi, M. J., Kashiwai, M., Ware, D. M., Megrey, B. A., Eslinger, D. L., Werner, F. E., Noguchi-Aita, M., Azumaya, T., Fujii, M., Hashimoto, S., Huang, D. J., Iizumi, H., Ishida, Y., Kang, S., Kantakov, G. A., Kim, H. C., Komatsu, K., Navrotsky, V. V., Smith, S. L., Tadokoro, K., Tsuda, A., Yamamura, O., Yamanaka, Y., Yokouchi, K., Yoshie, N., Zhang, J., Zuenko, Y. I., Zvalinsky, V. I., 2007. NEMURO–a lower trophic level model for the North Pacific marine ecosystem. Ecological Modelling 202 (1-2), 12–25.

Kyewalyanga, M., Platt, T., Sathyendranath, S., 1992. Ocean primary production calculated by spectral and broad-band models. Marine Ecology Progress Series 85, 171–185.

Kyewalyanga, M. N., Platt, T., Sathyendranath, S., 1997. Estimation of the photosynthetic action spectrum: implication for primary production models. Marine Ecological Progress Series 146, 207–223.

Laws, E. A., DiTullio, G. R., Redalje, D. G., 1987. High phytoplankton growth and production in the North Pacific subtropical gyre. Limnology and Oceanography 32, 905–918.

1080 Laws, E. A., Falkowski, P. G., Smith Jr, W. O., Ducklow, H., McCarth, J. J.,
1081 2000. Temperature effects on export production in the open ocean. Global Bio-
1082 geochemical Cycles 14, 1231–1246.
1083 Le Quéré, C., Harrison, S. P., Prentice, C. I., Buitenhuis, E. T., Aumont, O.,
1084 Bopp, L., Claustre, H., Cotrim Da Cunha, L., Geider, R., Giraud, X., Klaas,
1085 C., Kohfeld, K. E., Legendre, L., Manizza, M., Platt, T., Rivkin, R., Sathyen-
1086 dranath, S., Uitz, J., Watson, A. J., Wolf-Gladrow, D., 2005. Ecosystem dy-
1087 namics based on plankton functional types for global ocean biogeochemistry
1088 models. Global Change Biology 11, 2016–2040.
1089 Legendre, L., LeFevre, J., 1991. From individual plankton cells to pelagic marine
1090 ecosystems and to global biogeochemical cycles. In: Demers, S. (Ed.), Particle
1091 Analysis in Oceanography. Springer, Berlin, pp. 261–300.
1092 Longhurst, A., Sathyendranath, S., Platt, T., Caverhill, C., 1995. An estimate of
1093 global primary production in the ocean from satellite radiometer data. Journal
1094 of Plankton Research 17, 1245–1271.
1095 Lorenzo, L. M., Figueiras, F. G., Tilstone, G., Arbones, B., Mirón, I., 2004.
1096 Photosynthesis and light regime in the Azores Front region during summer:
1097 are light-saturated computations of primary production sufficient? Deep-Sea
1098 Research I 51, 1229–1244.
1099 Maloney, C. L., Field, J. G., 1991. The size-based dynamics of plankton food
1100 webs. I. A simulation model of carbon and nitrogen flows. Journal of Plankton
1101 Research 13 (5), 1003–1038.
1102 Marañón, E., 2009. Phytoplankton size structure. In: Steele, J. H., Turekian,

1103 K., Thorpe, S. A. (Eds.), Encyclopedia of Ocean Sciences. Academic Press,
1104 Oxford.
1105 Marañón, E., 2015. Cell size as a key determinant of phytoplankton metabolism
1106 and community structure. Annual Review of Marine Science 7, 241–264.
1107 Marañón, E., Cermeño, P., López-Sandoval, D. C., Rodríguez-Ramos, T., So-
1108 brino, C., Huete-Ortega, M., Blanco, J. M., Rodríguez, J., 2013. Unimodal
1109 size scaling of phytoplankton growth and the size dependence of nutrient up-
1110 take and use. Ecology Letters 16, 371–379.
1111 Marañón, E., Holligan, P. M., 1999. Photosynthetic parameters of phytoplankton
1112 from 50°N to 50°S in the Atlantic Ocean. Marine Ecological Progress Series
1113 176, 191–203.
1114 Marañón, E., Holligan, P. M., Barciela, R., González, N., Mouriño, B., Pazó,
1115 M. J., Varela, M., 2001. Patterns of phytoplankton size structure and pro-
1116 ductivity in contrasting open-ocean environments. Marine Ecological Progress
1117 Series 216, 43–56.
1118 Marañón, E., Holligan, P. M., Varela, M., Mouriño, B., Bale, A., 2000. Basin-
1119 scale variability of phytoplankton biomass, production and growth in the At-
1120 lantic Ocean. Deep Sea Research I 47, 825–857.
1121 Marinov, I., Doney, S. C., Lima, I. D., 2010. Response of ocean phytoplankton
1122 community structure to climate change over the 21st century: partitioning the
1123 effects of nutrients, temperature and light. Biogeosciences 7, 3941–3959.
1124 Maritorena, S., Fanton d'Andon, O. H., Mangin, A., Siegel, D. A., 2010. Merged
1125 satellite ocean color data products using a bio-optical model: Characteristics,

benefits and issues. Remote Sensing Environment 114, 1791–1804.

Markwardt, C. B., 2008. Non-linear least squares fitting in IDL with MPFIT. In: Bohlender, D., Dowler, P., Duran, D. (Eds.), Proceedings of the Astronomical Data Analysis Software and Systems XVIII, ASP Conference Series, Quebec, Canada, vol. 411. Astronomical Society of the Pacific, San Francisco.

Michaels, A. F., Silver, M. W., 1988. Primary production, sinking fluxes and the microbial food web. Deep-Sea Research I 35, 473–490.

Mignot, A., Claustre, H., Uitz, J., Poteau, A., D'Ortenzio, F., Xing, X., 2014. Understanding the seasonal dynamics of phytoplankton biomass and DCM in oligotrophic environments: a Bio-Argo float investigation. Global Biogeochemical Cycles 28, 856–876.

Moré, J., 1978. The Levenberg-Marquardt algorithm: implementation and theory. In: Numerical Analysis. Springer-Verlag, Berlin.

Morel, A., 1991. Light and marine photosynthesis: a spectral model with geochemical and climatological implications. Progress in Oceanography 26, 263–306.

Morel, A., Berthon, J. F., 1989. Surface pigments, algal biomass profiles, and potential production of the euphotic layer: Relationships reinvestigated in view of remote-sensing applications. Limnology and Oceanography 34, 1545–1562.

Morel, A., Huot, Y., Gentili, B., Werdell, P. J., Hooker, S. B., Franz, B. A., 2007. Examining the consistency of products derived from various ocean color sensors in open ocean (case 1) waters in the perspective of a multi-sensor

approach. Remote Sensing of Environment 111, 69–88.

Mouriño Carballido, B., Hojas, E., Cermeño, P., Chouciño, P., Fernández-Castro, B., Latasa, M., Marañón, E., Morán, X. A. G., Vidal, M., 2016. Nutrient supply controls picoplankton community structure during three contrasting seasons in the northwestern mediterranean sea. Marine Ecology Progress Series 543, 1–19.

Mouw, C. B., Yoder, J., 2005. Primary production calculations in the Mid-Atlantic Bight, including effects of phytoplankton community size structure. Limnology and Oceanography 50 (4), 1232–1243.

Müller, D., Krasemann, H., Brewin, R. J. W., Brockmann, C., Deschamps, P.-Y., Doerffer, R., Fomferra, N., Franz, B. A., Grant, M. G., Groom, S., Mélin, F., Platt, T., Regner, P., Sathyendranath, S., Steinmetz, F., Swinton, J., 2015a. The Ocean Colour Climate Change Initiative: I. An assessment of atmospheric correction algorithms based on in-situ measurements. Remote Sensing Environment 162, 242–256.

Müller, D., Krasemann, H., Brewin, R. J. W., Brockmann, C., Deschamps, P.-Y., Doerffer, R., Fomferra, N., Franz, B. A., Grant, M. G., Groom, S., Mélin, F., Platt, T., Regner, P., Sathyendranath, S., Steinmetz, F., Swinton, J., 2015b. The Ocean Colour Climate Change Initiative: II. Spatial and seasonal homogeneity of atmospheric correction algorithms. Remote Sensing Environment 162, 257–270.

NASA, June 2016. Seawifs vs. in situ.

URL http://seabass.gsfc.nasa.gov/seabasscgi/search.cgi?search_type=

1172 Platt, T. Caverhill, C., Sathyendranath, S., 1991. Basin-scale estimates of oceanic
1173 primary production by remote sensing: The North Atlantic. Journal of Geo-
1174 physical Research 96, 15,147–15,159.
1175 Platt, T., Gallegos, C. L., Harrison, W. G., 1980. Photoinhibition of photosyn-
1176 thesis in natural assemblages of marine phytoplankton. Journal of Marine Re-
1177 search 38, 687–701.
1178 Platt, T., Sathyendranath, S., 1988. Oceanic primary production: Estimation by
1179 remote sensing at local and regional scales. Science 241, 1613–1620.
1180 Platt, T., Sathyendranath, S., 1993. Estimators of primary production for inter-
1181 pretation of remotely sensed data on ocean color. Journal of Geophysical Re-
1182 search 98, 14,561–14,576.
1183 Platt, T., Sathyendranath, S., Forget, M.-H., White III, G. N., Caverhill, C.,
1184 Bouman, H., Devred, E., Son, S., 2008. Operational estimation of primary
1185 production at large geographical scales. Remote Sensing of Environment 112,
1186 3437–3448.
1187 Platt, T., Sathyendranath, S., Ravindran, P., 1990. Primary production by phy-
1188 toplankton: Analytic solutions for daily rates per unit area of water surface.
1189 Proceedings of the Royal Society of London Series B: Biological Sciences
1190 241, 101–111.
1191 Poulton, A. J., Holligan, P. M., Hickman, A., Kim, Y.-N., Adey, T. R., Stinch-
1192 combe, M. C., Holeton, C., Root, S., Woodward, E. M. S., 2006. Phytoplank-
1193 ton carbon fixation, chlorophyll-biomass and diagnostic pigments in the At-
1194 lantic Ocean. Deep Sea Research II 53, 1593–1610.

1195 Raven, J. A., 1994. Why are there no picoplanktonic O_2 evolvers with volumes
1196 less than 10^{-19} m^3? Journal of Plankton Research 16, 565–580.
1197 Rivkin, R. B., Putt, M., 1987. Diel periodicity of photosynthesis in polar phyto-
1198 plankton: Influence on primary production. Science 238, 1285–1288.
1199 Robinson, C., Poulton, A. J., Holligan, P. M., Baker, A. R., Forster, G., Gist, N.,
1200 Jickells, T. D., Malin, G., Upstill-Goddardd, R., Williams, R. G., Woodward,
1201 E. M. S., Zubkov, M. V., 2006. The Atlantic Meridional Transect (AMT) Pro-
1202 gramme: a contextual view 1995-2005. Deep Sea Research II 53, 1485–1515.
1203 Robinson, C., Serret, P., Tilstone, G., Teira, E., Zubkov, M. V., Rees, A. P.,
1204 Woodward, E. M. S., 2002. Plankton respiration in the Eastern Atlantic Ocean.
1205 Deep Sea Research I 49, 787–813.
1206 Sathyendranath, S., Krasemann, H., 2014. Climate Assessment Report: Ocean
1207 Colour Climate Change Initiative (OC-CCI) - Phase One.
1208 URL http://www.esa-oceancolour-cci.org/?q=documents
1209 Sathyendranath, S., Longhurst, A., Caverhill, C. M., Platt, T., 1995. Regionally
1210 and seasonally differentiated primary production in the North Atlantic. Deep
1211 Sea Research I 42, 1773–1802.
1212 Sathyendranath, S., Platt, T., 1988. The spectral irradiance field at the surface and
1213 interior of the ocean: A model for applications in oceanography and remote
1214 sensing. Journal of Geophysical Research 93, 9270–9280.
1215 Sathyendranath, S., Platt, T., 1989. Computation of aquatic primary production:
1216 extended formalism to include effect of angular and spectral distribution of
1217 light. Limnology and Oceanography 34, 188–198.

1218 Sathyendranath, S., Platt, T., 2007. Spectral effects in bio-optical control on the
1219 ocean system. Oceanologia 49, 5–39.
1220 Sathyendranath, S., Stuart, V., Cota, G., Maas, H., Platt, T., 2001. Remote sens-
1221 ing of phytoplankton pigments: a comparison of empirical and theoretical
1222 approaches. International Journal of Remote Sensing 22, 249–273.
1223 Sathyendranath, S., Stuart, V., Nair, A., Oka, K., Nakane, T., Bouman, H., For-
1224 get, H.-M., Maass, H., Platt, T., 2009. Carbon-to-chlorophyll ratio and growth
1225 rate of phytoplankton in the sea. Marine Ecological Progress Series 383, 73–
1226 84.
1227 Sathyendranath, S., Watts, L., Devred, E., Platt, T., Caverhill, C., Maass, H.,
1228 2004. Discrimination of diatoms from other phytoplankton using ocean-colour
1229 data. Marine Ecological Progress Series 272, 59–68.
1230 Saux Picart, S., Sathyendranath, S., Dowell, M., Moore, T., Platt, T., 2014. Re-
1231 mote sensing of assimilation number for marine phytoplankton. Remote Sens-
1232 ing Environment 146, 87–96.
1233 Sauzède, R., Claustre, H., Jamet, C., Uitz, J., Ras, J., Mignot, A., D'Ortenzio, F.,
1234 2015. Retrieving the vertical distribution of chlorophyll a concentration and
1235 phytoplankton community composition from in situ fluorescence profiles: A
1236 method based on a neural network with potential for global-scale applications.
1237 Journal of Geophysical Research 119, 451–470.
1238 Silió-Calzada, A., Bricaud, A., Uitz, J., Gentili, B., 2008. Estimation of new
1239 primary production in the Benguela upwelling area, using ENVISAT satellite
1240 data and a model dependent on the phytoplankton community size structure.

1241 Journal of Geophysical Research 113, C11023.
1242 Smyth, T., Tilstone, G., Groom, S., 2005. Integration of radiative transfer into
1243 satellite models of ocean primary production. Journal of Geophysical Re-
1244 search 110, C10014.
1245 Tilstone, G., Figueiras, F. G., Lorenzo, L. M., Arbones, B., 2003. Phytoplankton
1246 composition, photosynthesis and primary production during different hydro-
1247 graphic conditions at the Northwest Iberian upwelling system. Marine Eco-
1248 logical Progress Series 252, 89–104.
1249 Tilstone, G., Lange, P. K., Misra, A., Brewin, R. J. W., Cain, T., Airs, R., Ac-
1250 cepted. Significance of micro-phytoplankton primary production in the At-
1251 lantic Ocean. Progress in Oceanography.
1252 Tilstone, G., Smyth, T., Poulton, A., Hutson, R., 2009. Measured and remotely
1253 sensed estimates of primary production in the Atlantic Ocean from 1998 to
1254 2005. Deep Sea Research II 56, 918–930.
1255 Uitz, J., Claustre, H., Brian Griffiths, F., Ras, J., Garcia, N., Sandroni, V., 2009.
1256 A phytoplankton class-specific primary production model applied to the Ker-
1257 guelen Islands region (Southern Ocean). Deep-Sea Research I 56, 541–560.
1258 Uitz, J., Claustre, H., Gentili, B., Stramski, D., 2010. Phytoplankton class-
1259 specific primary production in the world's oceans: Seasonal and interan-
1260 nual variability from satellite observations. Global Biogeochemical Cycles 24,
1261 GB3016.
1262 Uitz, J., Claustre, H., Morel, A., Hooker, S. B., 2006. Vertical distribution of
1263 phytoplankton communities in open ocean: an assessment based on surface

chlorophyll. Journal of Geophysical Research 111, C08005.

Uitz, J., Huot, Y., Bruyant, F., Babin, M., Claustre, H., 2008. Relating phytoplankton photophysiological properties to community structure on large scales. Limnology and Oceanography 53 (2), 614–630.

Uitz, J., Stramski, D., Gentili, B., D'Ortenzio, F., Claustre, H., 2012. Estimates of phytoplankton class-specific and total primary production in the Mediterranean Sea from satellite ocean color observations. Global Biogeochemical Cycles 26, GB2024.

Veldhuis, M., Timmermans, K. R., Croot, P., Wagt, B., 2005. Picophytoplankton; a comparative study of their biochemical composition and photosynthetic properties. Journal of Sea Research 53, 7–24.

Ward, B. A., 2015. Temperature-Correlated Changes in Phytoplankton Community Structure Are Restricted to Polar Waters. PLoS ONE 10 (8), e0135581.

Ward, B. A., Dutkiewicz, S., Jahn, O., Follows, M. J., 2012. A size-structured food-web model for the global ocean. Limnology and Oceanography 57 (6), 1877–1891.

Xiao, Y., Friedrichs, M. A. M., 2014. The assimilation of satellite-derived data into a one-dimensional lower trophic level marine ecosystem model. Journal of Geophysical Research 119, 2691–2712.

Xing, X., Morel, A., Claustre, H., Antoine, D., D'Ortenzio, F., Poteau, A., Mignot, A., 2011. Combined processing and mutual interpretation of radiometry and fluorimetry from autonomous profiling Bio-Argo floats. The retrieval of Chlorophyll a. Journal of Geophysical Research 116, C06020.

1287 Yentch, C. S., Ryther, J. H., 1957. Short-Term Variations in Phytoplankton
1288 Chlorophyll and Their Significance. Limnology and Oceanography 2, 140–
1289 142.
1290 Zubkov, M., Sleigh, M. A., Burkill, P. H., Leakey, R. J. G., 2000. Picoplank-
1291 ton community structure on the Atlantic Meridional Transect: a comparison
1292 between seasons. Progress in Oceanography 45, 369–386.

Table 1: Symbols and definitions.

Symbol	Definition	Units
$\tilde{a}_{p,i}$	Average phytoplankton absorption coefficient of size class i	m^{-1}
$\tilde{a}_{T,i}$	Weighted average phytoplankton absorption coefficient of size class i	m^{-1}
$a^B_{p,i}(\lambda)$	Chlorophyll-specific phytoplankton absorption coefficient of size class i	m^2 [mg B]$^{-1}$
B	Chlorophyll concentration	mg
B_i	Chlorophyll concentration for size class i	mg
$B^m_{1,2}$	Asymptotic maximum value of $B_{1,2}$ (cells $<10\,\mu$m)	mg
B^m_1	Asymptotic maximum value of B_1 (cells $<2\,\mu$m)	mg
B_s	Surface chlorophyll concentration (average concentration within the mixed-layer)	mg
B^{Bs}	Chlorophyll concentration in a vertical profile normalised to surface value	dimensionless
B^{Bs}_m	Maximum chlorophyll concentration in a vertical profile normalised to surface value	dimensionless
C	Phytoplankton Carbon	mg
D	Daylength	h
DOY	Day of year	d
E	Empirical coefficient used to estimate B^{Bs}_m from B_s	dimensionless
F	Empirical coefficient used to estimate B^{Bs}_m from B_s	dimensionless
G	Empirical coefficient used to estimate ζ_m from B_s	dimensionless
H	Empirical coefficient used to estimate ζ_m from B_s	dimensionless
i	Size class of phytoplankton (i=1 for cells $<2\,\mu$m; i=2 for cells 2-10 μm; and i=3 for cells $>10\,\mu$m)	μm
I	Total irradiance from 400-700nm	μmol quanta m^{-2} s^{-1}
I_K	Photoadaptation parameter ($P^B_{m,i}/\alpha^B_i$)	μmol quanta m^{-2} s^{-1}
$I_m(0+)$	Total irradiance from 400-700nm at mid-day just above the surface	μmol quanta m^{-2} s^{-1}
$I_m(0-)$	Total irradiance from 400-700nm at mid-day just below the surface	μmol quanta m^{-2} s^{-1}
$I_T(\lambda)$	Spectral irradiance from 400-700nm of a lamp (either Tungsten or LED)	μmol quanta m^{-2} s^{-1}
J	Intercept of a Type-2 regression on $\log_{10}$-transformed P_i from model and *in situ* data	dimensionless
K	Diffuse attenuation coefficient for I	m^{-1}
K_c	Constant background K	m^{-1}
K_v	Variable component of K related to non-water optical constituents	m^{-1}
K_{Zp}	Average diffuse attenuation coefficient for I within the euphotic zone	m^{-1}
N	Number of samples	counts
P	Total primary production	mg C
P_i	Primary production for size class i	mg C
P^B	Total primary production normalised to chlorophyll concentration	mg C (mg B)$^{-1}$
P^B_i	Total primary production normalised to chlorophyll concentration for size class i	mg C (mg B)$^{-1}$
P^B_m	The assimilation number of the light-saturation curve	mg C (mg B)$^{-1}$ h^{-1}
$P^B_{m,i}$	The assimilation number of the light-saturation curve of size class i	mg C (mg B)$^{-1}$ h^{-1}
$P^{Bs}_{m,i}$	The assimilation number of the light-saturation curve of size class i at the surface	mg C (mg B)$^{-1}$ h^{-1}
PAR	Photosynthetically available radiation	Einstein m^{-2} d^{-1}
$q_{0\to3}$	Empirical coefficients used to compute Z_p from B_s	dimensionless
r	Pearson correlation coefficient	dimensionless
$S_{1,2}$	Slope determining the increase in $B_{1,2}$ (cells $<10\,\mu$m) with B	dimensionless
S_1	Slope determining the increase in B_1 (cells $<2\,\mu$m) with B	dimensionless
S^{Bs}	Slope of change in B^{Bs} with ζ	dimensionless
S^P_i	Slope of change in $P^{Bs}_{m,i}$ with ζ	dimensionless
S_T	Slope of a Type-2 regression on $\log_{10}$-transformed P_i two datasets (e.g. model and *in situ*)	dimensionless
S^α_i	Slope of change in α^{Bs}_i with ζ	dimensionless
t	Time	h
W_i	Lamp correction factor applied to α^B_i for each size class	dimensionless
z	Geometric depth	m
Z_m	Mixed-layer depth	m
Z_p	Euphotic depth	m
α^B	The initial slope of a P^B and I curve	mg C (mg B)$^{-1}$ h^{-1} (μmol quanta m^{-2} s^{-1})$^{-1}$
α^B_i	The initial slope of a P^B and I curve of size class i	mg C (mg B)$^{-1}$ h^{-1} (μmol quanta m^{-2} s^{-1})$^{-1}$
α^{Bs}_i	The initial slope of a P^B and I curve of size class i at the surface	mg C (mg B)$^{-1}$ h^{-1} (μmol quanta m^{-2} s^{-1})$^{-1}$
δ	Bias between $\log_{10}$-transformed P_i from two datasets (e.g. model and *in situ*)	dimensionless
Δ	Centre-pattern (or unbiased) root mean square error on $\log_{10}$-transformed P_i from two datasets (e.g. model and *in situ*) and standard deviation on Monte Carlo simulation output	dimensionless
Ψ	Root mean square error on $\log_{10}$-transformed P_i from two datasets (e.g. model and *in situ*)	dimensionless
σ	The width of the B^{Bs}_m peak	dimensionless
ξ	Empirical parameter designed to serve a linear transition in B from mixed to stratified waters	dimensionless
ζ	Dimensionless depth (z/Z_p)	dimensionless
ζ_m	Dimensionless depth at which B^{Bs}_m occurs	dimensionless

Table 2: Model parameters used to estimate size-fractionated primary production in Eq. 3. Standard deviation on model parameters were estimated using a Monte Carlo approach using 1000 bootstraps.

Output variable	Input variable(s)	Eq.	Parameter	Value	Standard deviation	Parameter Units
Euphotic	B_s	3	q_a	1.525	0.079	-
Depth			q_b	−0.488	0.133	-
(Z_p)			q_c	−0.020	0.024	-
			q_d	0.013	0.036	-
Total	B_s, Z_p & Z_m	5	S^{Bs}	0.325	0.846	-
Chlorophyll			B_m^{Bs}	$10^{(\log_{10}(B_s)E+F)}$	-	-
($B(z)$)			E	−0.785	0.077	-
			F	−0.285	0.081	-
			ζ_m	$\log_{10}(B_s)G + H$	-	-
			G	−0.219	0.077	-
			H	0.719	0.073	-
			σ	0.295	0.242	-
			ξ	$(Z_p/Z_m - 1.0)/(1.5 - 1.0)$	-	-
Size-specific	$B(z)$	6-9	$B_{1,2}^m$	1.28	0.205	mg m^{-3}
Chlorophyll			B_1^m	0.60	0.099	mg m^{-3}
($B_i(z)$)			$S_{1,2}$	0.75	0.111	-
			S_1	1.21	0.198	-
Size-specific	Z_p	13	$P_{m,1}^{Bs}$	3.46	0.80	mg C (mg B)$^{-1}$ h^{-1}
assimilation			$P_{m,2}^{Bs}$	5.13	0.94	mg C (mg B)$^{-1}$ h^{-1}
number			$P_{m,3}^{Bs}$	6.05	0.98	mg C (mg B)$^{-1}$ h^{-1}
($P_{m,i}^B$)			S_1^P	0.68	0.31	-
			S_2^P	0.59	0.29	-
			S_3^P	0.35	0.27	-
Size-specific	Z_p	14	α_1^{Bs}	0.011	0.001	mg C (mg B)$^{-1}$ h^{-1} (μmol quanta m^{-2} s^{-1})$^{-1}$
initial slope			α_2^{Bs}	0.014	0.003	mg C (mg B)$^{-1}$ h^{-1} (μmol quanta m^{-2} s^{-1})$^{-1}$
(α_i^B)			α_3^{Bs}	0.016	0.004	mg C (mg B)$^{-1}$ h^{-1} (μmol quanta m^{-2} s^{-1})$^{-1}$
			S_1^α	−0.32	0.17	-
			S_2^α	−0.12	0.23	-
			S_3^α	−0.07	0.30	-
Diffuse attenuation coefficient (K)	$B(z)$, Z_p & K_c	3, 18 19	-	-	-	-
Irradiance (I)	PAR, D & K	17 18, 18 19	-	-	-	-

Table 3: Basin scale estimates of annual size-fractionated production for 2007 in the Atlantic Ocean, compared with climatological estimates from the study of Uitz et al. (2010). The north and south boundaries of the Atlantic were assigned at 70°N and 50°S respectively, as with Uitz et al. (2010).

Region	**Study**	**%P <2μm**	**%P >2μm**	P_1 **[GtC y^{-1}]**	$P_{2,3}$ **[GtC y^{-1}]**	P **[GtC y^{-1}]**
Atlantic Ocean	This study[#]	47.0	53.0	3.7	4.2	7.9
North Atlantic	This study[#]	45.0	55.0	2.1	2.5	4.6
South Atlantic	This study[#]	50.0	50.0	1.6	1.7	3.3
Atlantic Ocean	Uitz et al. (2010)	21.0	79.0	2.5	9.6	12.2
North Atlantic	Uitz et al. (2010)	20.0	80.0	1.4	5.8	7.2
South Atlantic	Uitz et al. (2010)	22.0	78.0	1.1	3.9	5.0

[#] Monte Carlo simulations suggest the uncertainty (standard deviation) in annual estimates of %P <2μm and %P >2μm to be <1%, and for P, P_1 and $P_{2,3}$ <0.1 GtC y^{-1}. The random error introduced by these simulations is averaged out when integrating over space and time, resulting in small errors in annual production estimates. However, systematic errors in model parameters are likely to increase this uncertainty. Validation results suggest low systematic errors (δ) in P, P_1 and $P_{2,3}$ (see Fig. 12).

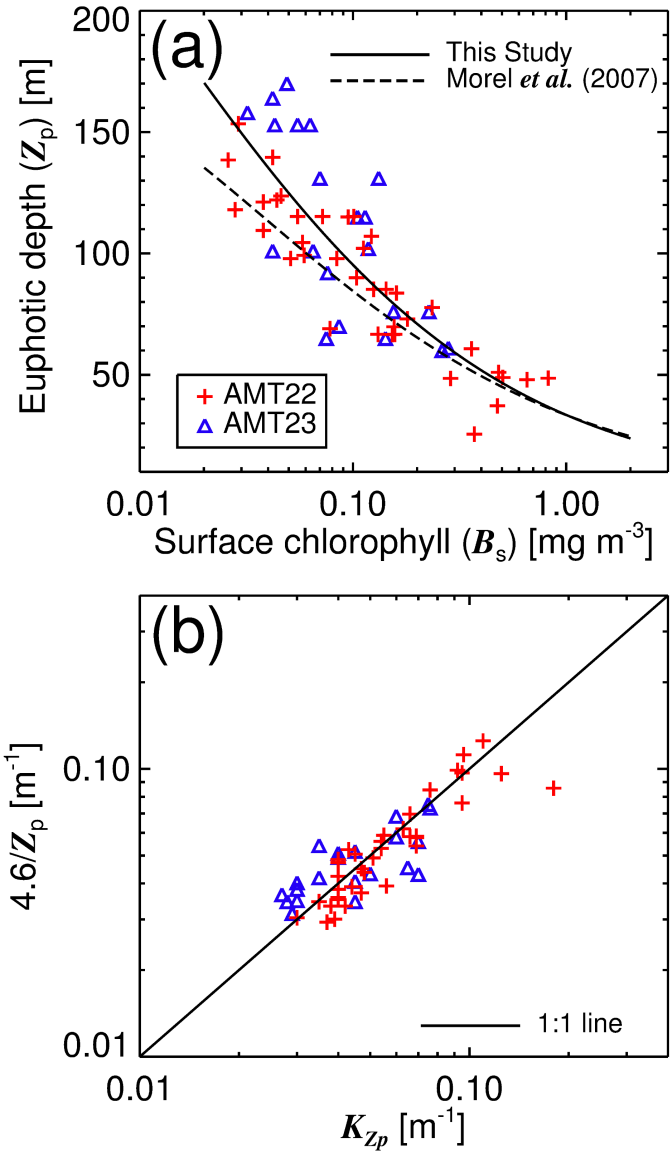

Figure 1: (a) Euphotic depth (Z_p) plotted as a function of surface chlorophyll concentration (B_s) for AMT 22 and 23 cruises. (b) $4.6/Z_p$ estimated as a function of B_s using Eq. 3 and plotted against the average diffuse attenuation coefficient in the euphotic zone K_{Zp}.

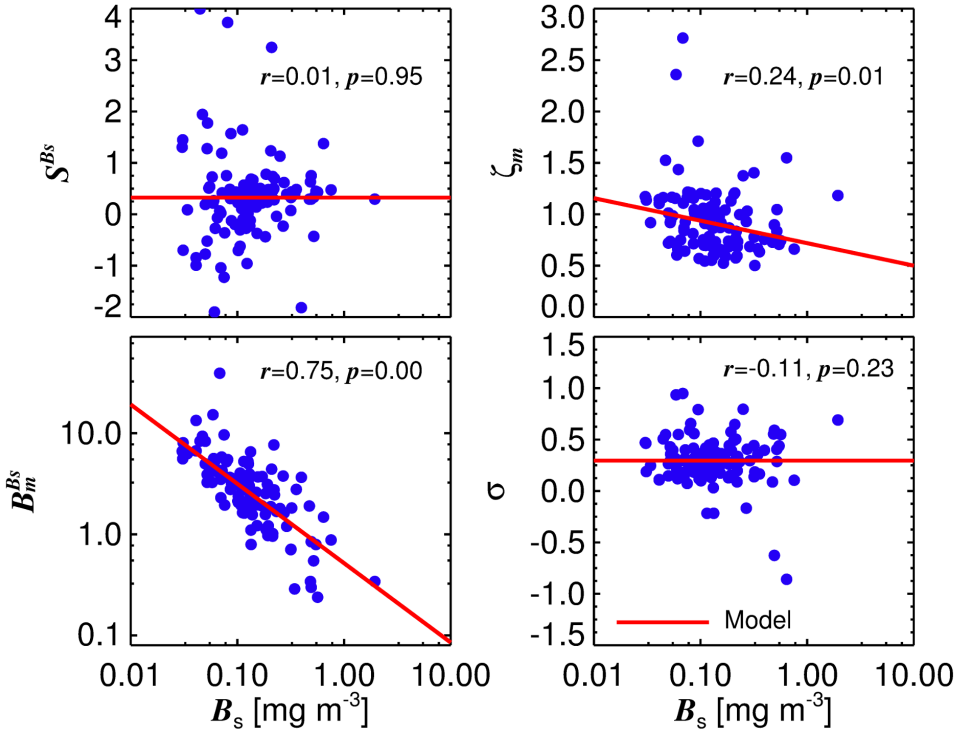

Figure 2: Retrieved model parameters for Eq. 4 plotted as a function of surface chlorophyll (B_s), following parameterisation of Eq. 4 to AMT HPLC chlorophyll profiles. S^{B_s} represents a background linear decrease with dimensionless depth (ζ), $B_m^{B_s}$ the maximum value of the normalised biomass profile (B^{B_s}), ζ_m the dimensionless depth at which $B_m^{B_s}$ occurs, and σ the width of the $B_m^{B_s}$ peak.

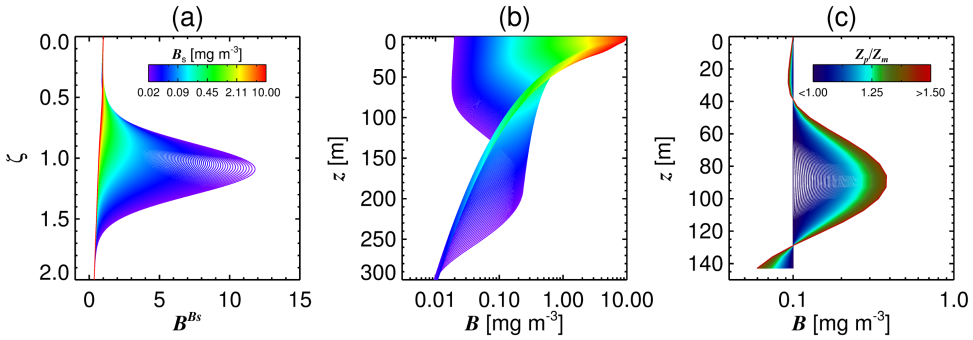

Figure 3: (a) Variations in the normalised biomass profile ($B^{B_s}(\zeta)$) as a function of surface chlorophyll (B_s) for stratified environments (Eq. 4), (b) reconstructed total chlorophyll ($B(z)$) for stratified environments as a function of B_s, and (c) an illustration the change in the total chlorophyll profile ($B(z)$) from stratified to mixed waters (ratio of euphotic depth (Z_p) to mixed-layer depth (Z_m)), where $B_s = 0.1$.

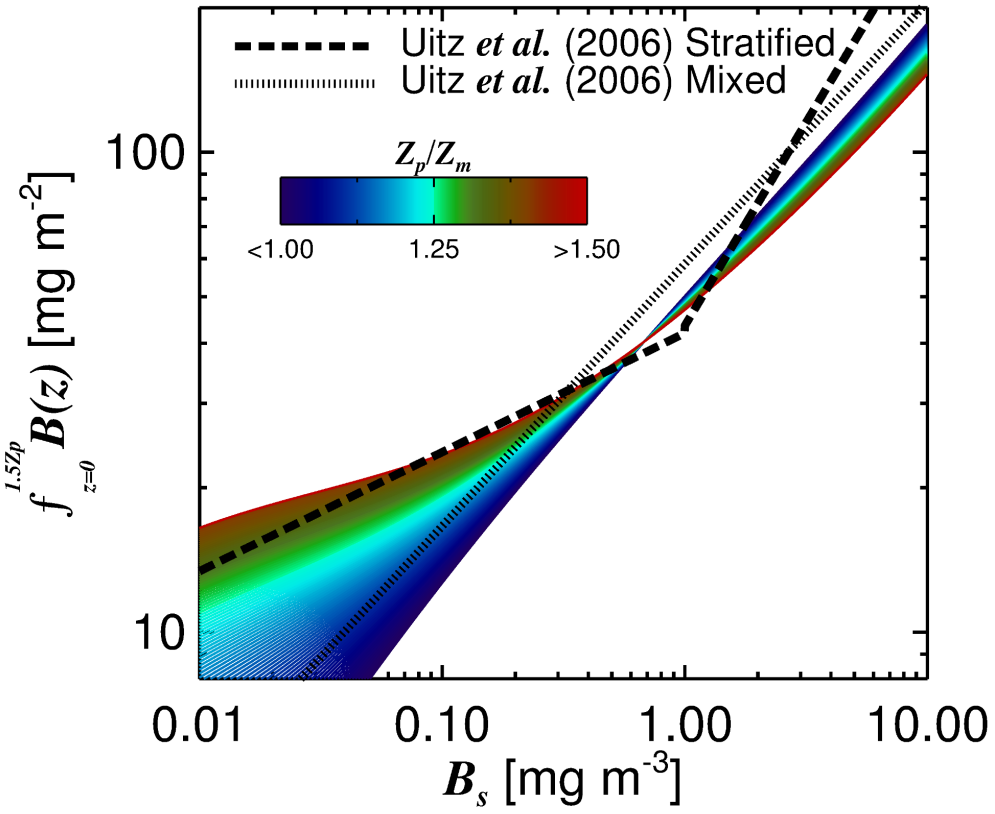

Figure 4: Integrated chlorophyll, computed by vertical integration of Eq. 5, for both mixed and stratified waters (ratio of euphotic depth (Z_p) to mixed-layer depth (Z_m)), as a function of surface chlorophyll (B_s).

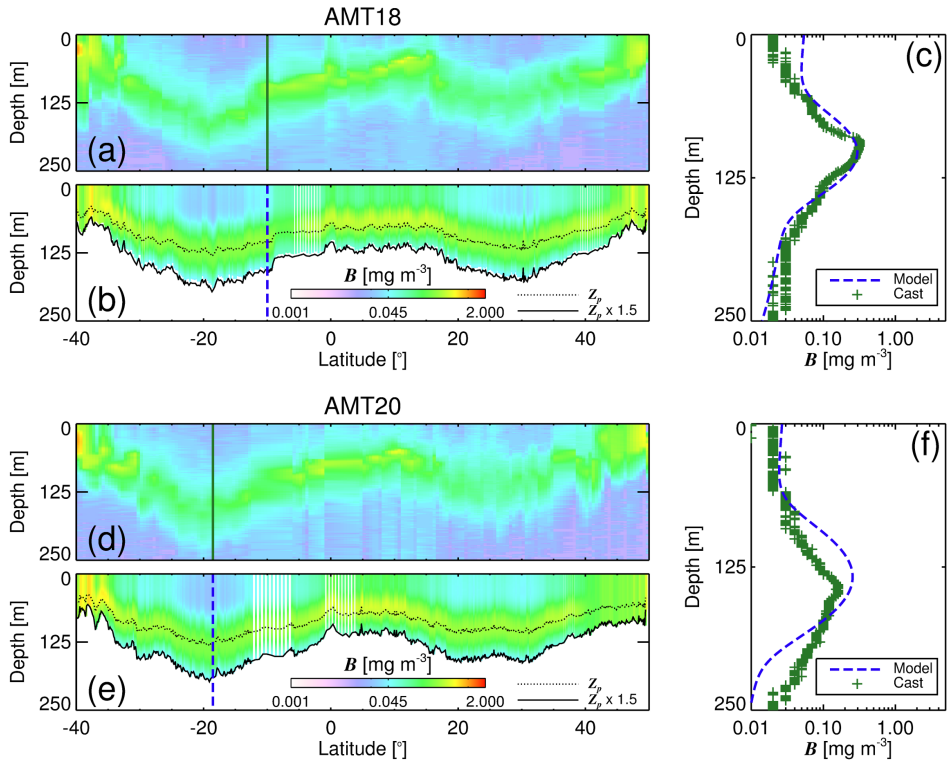

Figure 5: (a) Total chlorophyll profile ($B(z)$) derived from *in vivo* fluorescence on a CTD during the AMT 18 cruise (4th October to 10th November 2008). (b) $B(z)$ estimated using Eq. 5, using along-track satellite monthly surface chlorophyll (B_s) for October 2008 as input (ESA OC-CCI data) and mixed-layer depth from a monthly climatology for October (de Boyer Montégut et al., 2004). (c) An example of a profile from the satellite estimate (b) with a profile from the CTD (a) at the same location. (d) $B(z)$ derived from *in vivo* fluorescence on a CTD during the AMT 20 cruise (12th October to 25th November 2010). (e) $B(z)$ estimated using Eq. 5, using along-track satellite monthly B_s for November 2010 as input (ESA OC-CCI data) and mixed-layer depth from a monthly climatology for November (de Boyer Montégut et al., 2004). (f) An example of a profile from the satellite estimate (e) with a profile from the CTD (d) at the same location.

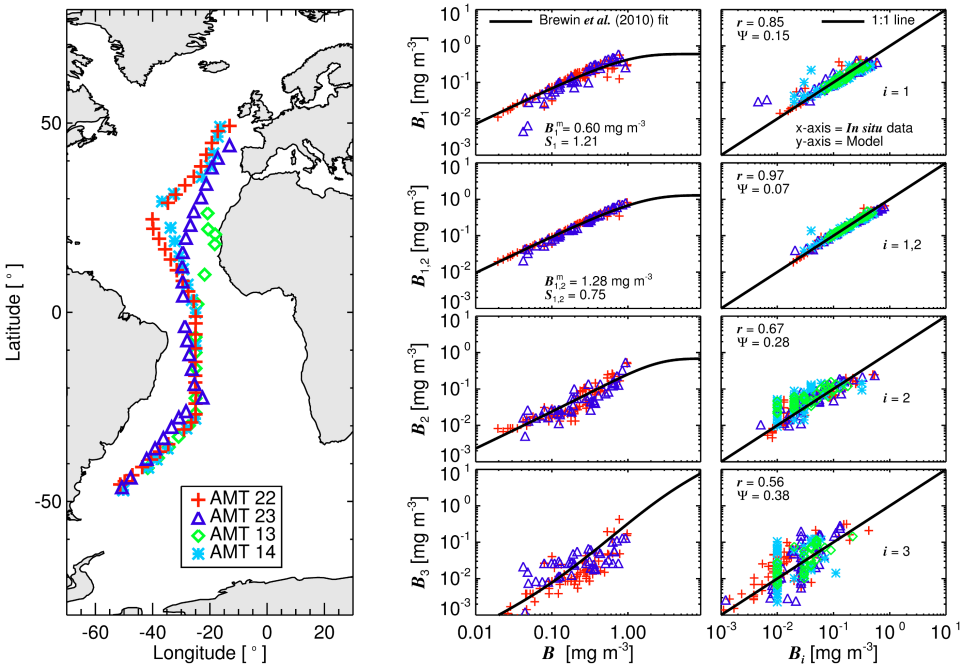

Figure 6: Geographical distribution of size-fractionated chlorophyll data for AMT cruises 13, 14, 22 and 23. Size-fractionated chlorophyll (B_i) is plotted as a function of total chlorophyll on AMT 22 and 23 cruises, with the Brewin et al. (2010b) model fitted to the data overlain (Table 2 parameters, where $B^m_{1,2}$ and B^m_1 are the asymptotic maximum values for the associated size classes (<10 μm and <2 μm respectively) and $S_{1,2}$ and S_1 determines the increase in size-fractionated chlorophyll (<10 μm and <2 μm respectively) with increasing total chlorophyll (B)), and the model is compared with independent size-fractionated chlorophyll from AMT 13 and 14, when applying the model to the total chlorophyll concentration (B). r is the Pearson correlation coefficient and Ψ the root mean square error, both computed comparing $\log_{10}$-transformed modelled and *in situ* B_i.

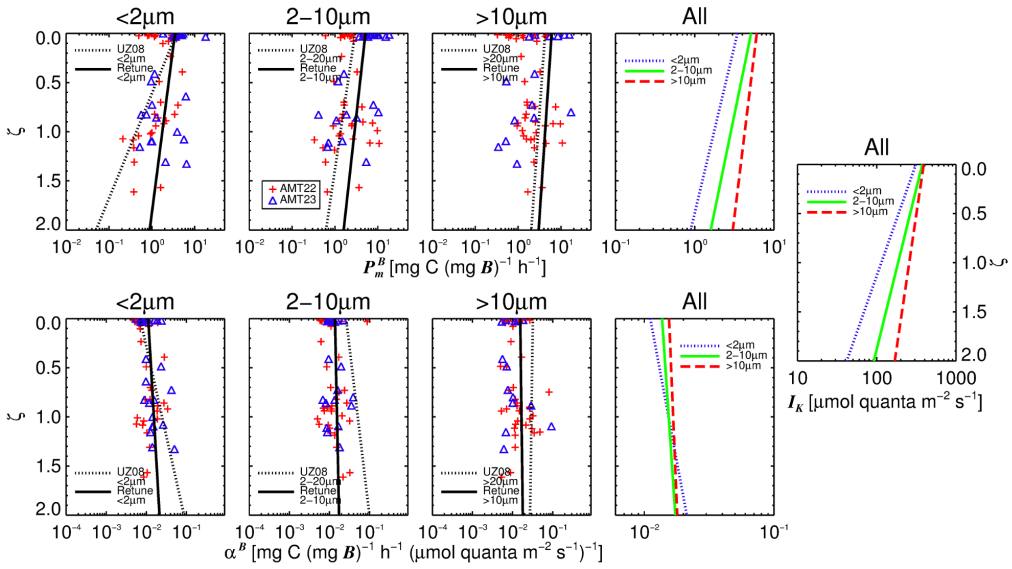

Figure 7: Relationships between the assimilation number ($P^B_{m,i}$) and dimensionless depth (ζ), and the initial slope (α^B_i) and ζ, for the three size classes, together with the relationships proposed by Uitz et al. (2008) and those used here (by retuning the Uitz et al. (2008) equations to AMT data). The photoadaptation parameter (I_k), computed as $P^B_{m,i}/\alpha^B_i$, is plotted with ζ.

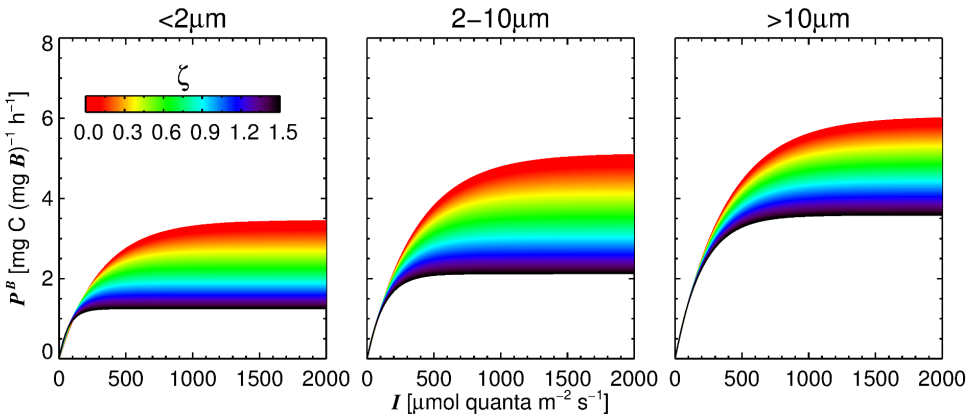

Figure 8: Normalised primary production (P^B) as a function of irradiance (I) for each size class in the size-fractionated primary production model, based on Eq. 13 and 14, for a variety of dimensionless depths (ζ).

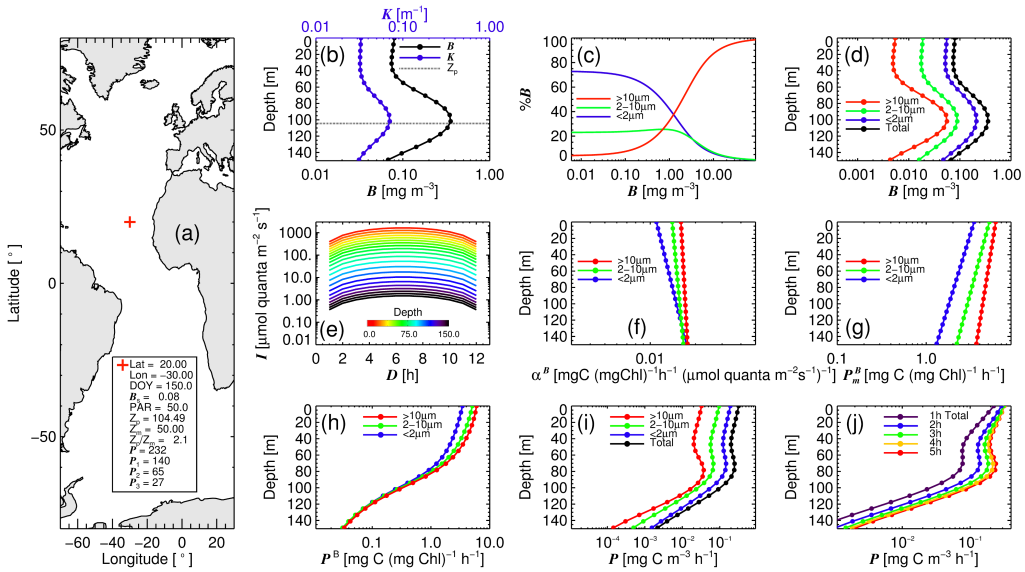

Figure 9: Size-fractionated primary production example (see Table 2 for list of symbols): (a) Input data and estimates of size-fractionated primary production; (b) vertical biomass profile $B(z)$ and $K(z)$ profile; (c) illustration of the model of Brewin et al. (2010b) partitioning total biomass (B) into the three size fractions; (d) the biomass profiles of the three size classes and total biomass; (e) the irradiance field ($I(z,t)$) modelled over the daylength (D) and depth (z); (f) depth variations in α^B for each size class; (g) depth variations in P^B_m for each size class; (h) the vertical profile of biomass-normalised production for the three size classes at noon (hour 6); (h) vertical profile of production for the three size classes and total (sum of the three size classes) at noon (hour 6); and (j) total production (sum of the three size classes) from hours 1 through to hour 6 of daylength (D).

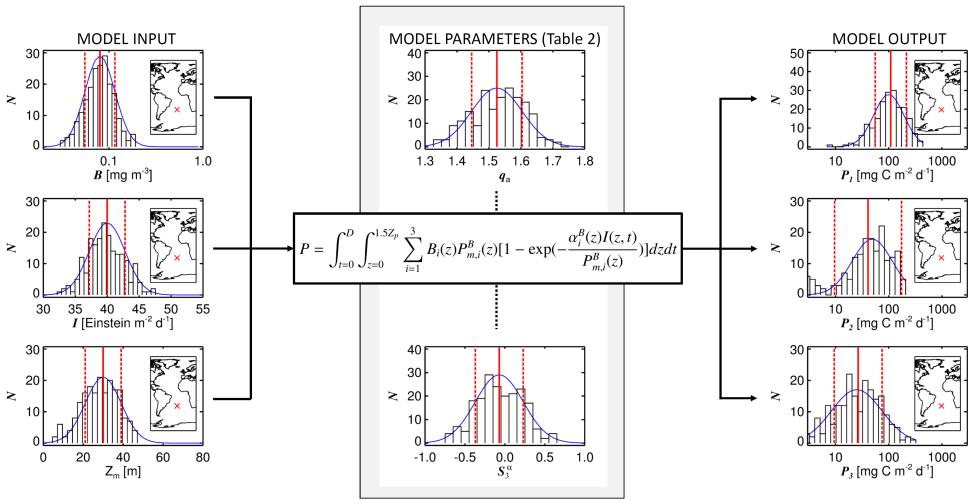

Figure 10: Example of a Monte Carlo simulation of the production model in the South Atlantic Gyre on the 30th May (latitude = −20°, longitude = −30°), where $B = 0.08\,\mathrm{mg\,m^{-3}}$, $I = 40$ Einstein $\mathrm{m^{-2}\,d^{-1}}$ and $Z_m = 30\,\mathrm{m}$. Model input is shown on the left, red lines represent the values of the input, dashed lines the input ± the standard deviation (uncertainty), blue line the Gaussian distribution derived from the input and standard deviation, and the back histogram shows the random allocation of 200 different model inputs taken from the Gaussian distribution. An example of histograms of two model parameters (Table 2) is shown in the centre, where the red lines represent the parameter value (Table 2), dashed lines the parameter value ± the standard deviation (Table 2), blue line the Gaussian distribution derived from the parameter value ± the standard deviation, and the back histogram shows the random allocation of 200 different parameters from the Gaussian distribution. Whereas two parameters are shown in the figure, all parameters were varied in the simulation. The right part of the figure shows a black histogram of the 200 possible model outputs from the Monte Carlo simulation, for each size class, where the red lines represent the median output value, dashed lines the median output value ± the standard deviation (Δ, in $\log_{10}$ space), and blue line shows a fitted Gaussian distribution of the output data.

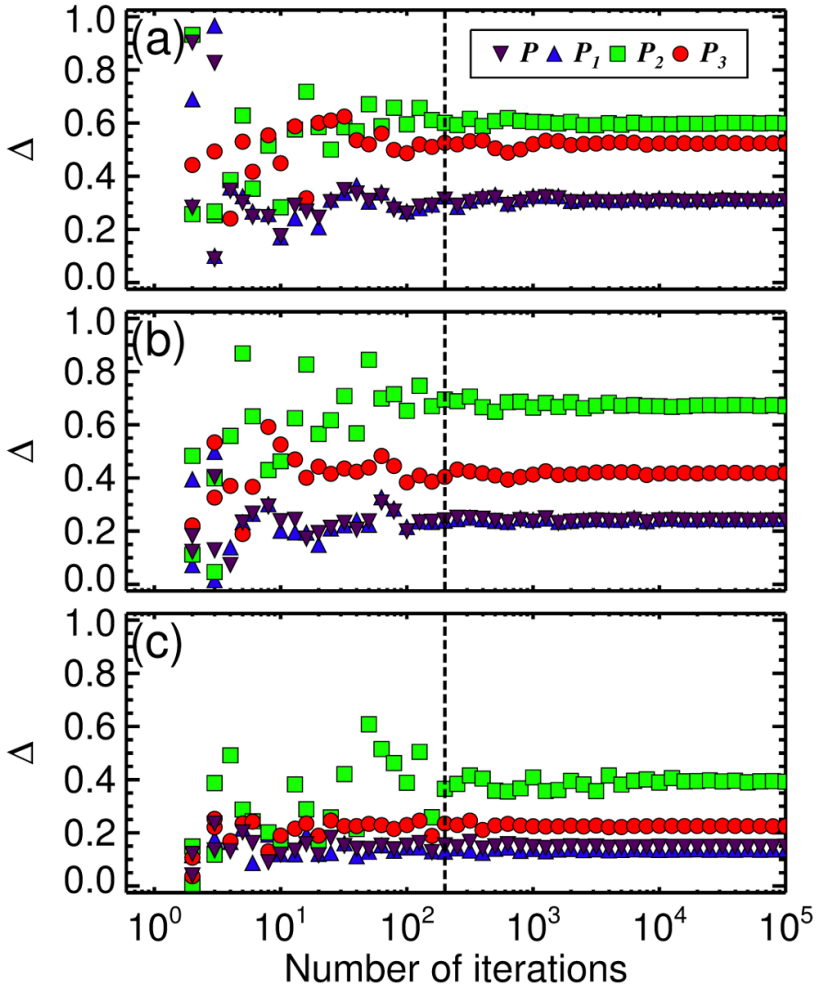

Figure 11: The standard deviation (Δ, in $\log_{10}$ space) for production in each size class (P_1, P_2, and P_3), and total production (P), from the Monte Carlo simulations, as a function of the number of iterations. (a) Show an example from the South Atlantic Gyre on the 10$^{\text{th}}$ January, where latitude = $-20°$, longitude = $-30°$, $B = 0.05\,\text{mg}\,\text{m}^{-3}$, $I = 55$ Einstein $\text{m}^{-2}\,\text{d}^{-1}$ and $Z_m = 30\,\text{m}$. (b) Shows an example from the equatorial Atlantic on the 19$^{\text{th}}$ August, where latitude = $0°$, longitude = $-30°$, $B = 0.2\,\text{mg}\,\text{m}^{-3}$, $I = 40$ Einstein $\text{m}^{-2}\,\text{d}^{-1}$ and $Z_m = 50\,\text{m}$. (c) Shows an example from the North Atlantic on the 10$^{\text{th}}$ April, where latitude = $45°$, longitude = $-30°$, $B = 2.0\,\text{mg}\,\text{m}^{-3}$, $I = 10$ Einstein $\text{m}^{-2}\,\text{d}^{-1}$ and $Z_m = 100\,\text{m}$. In all cases Δ stabilises at around 200 iterations.

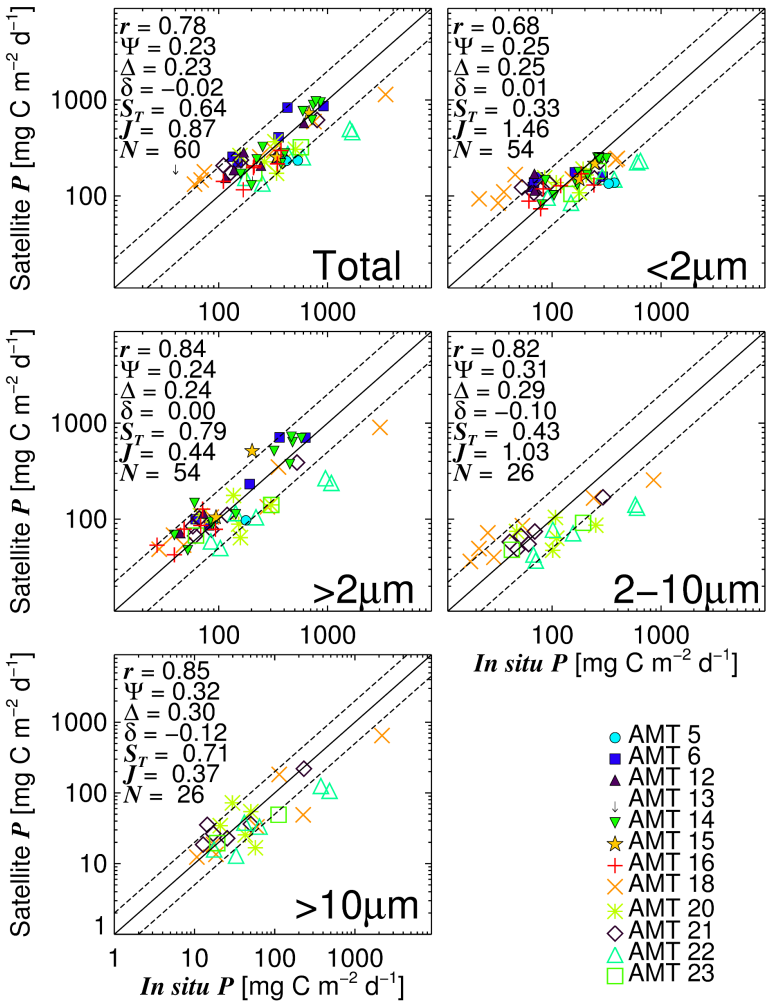

Figure 12: Comparisons of total production (P) and size-fractionated production (P_i) from satellite data using Eq. 2, and *in situ* data from a series of AMT cruises. The Pearson correlation coefficient (r), the root mean square error (Ψ), the average bias between model and measurement (δ), the centre-pattern (or unbiased) root mean square error (Δ), the slope (S_T) and intercept (J) of a Type-2 regression, and number of samples (N) are provided for each size class. Solid line represents 1:1 line and dashed lines ±30% $\log_{10}$ production.

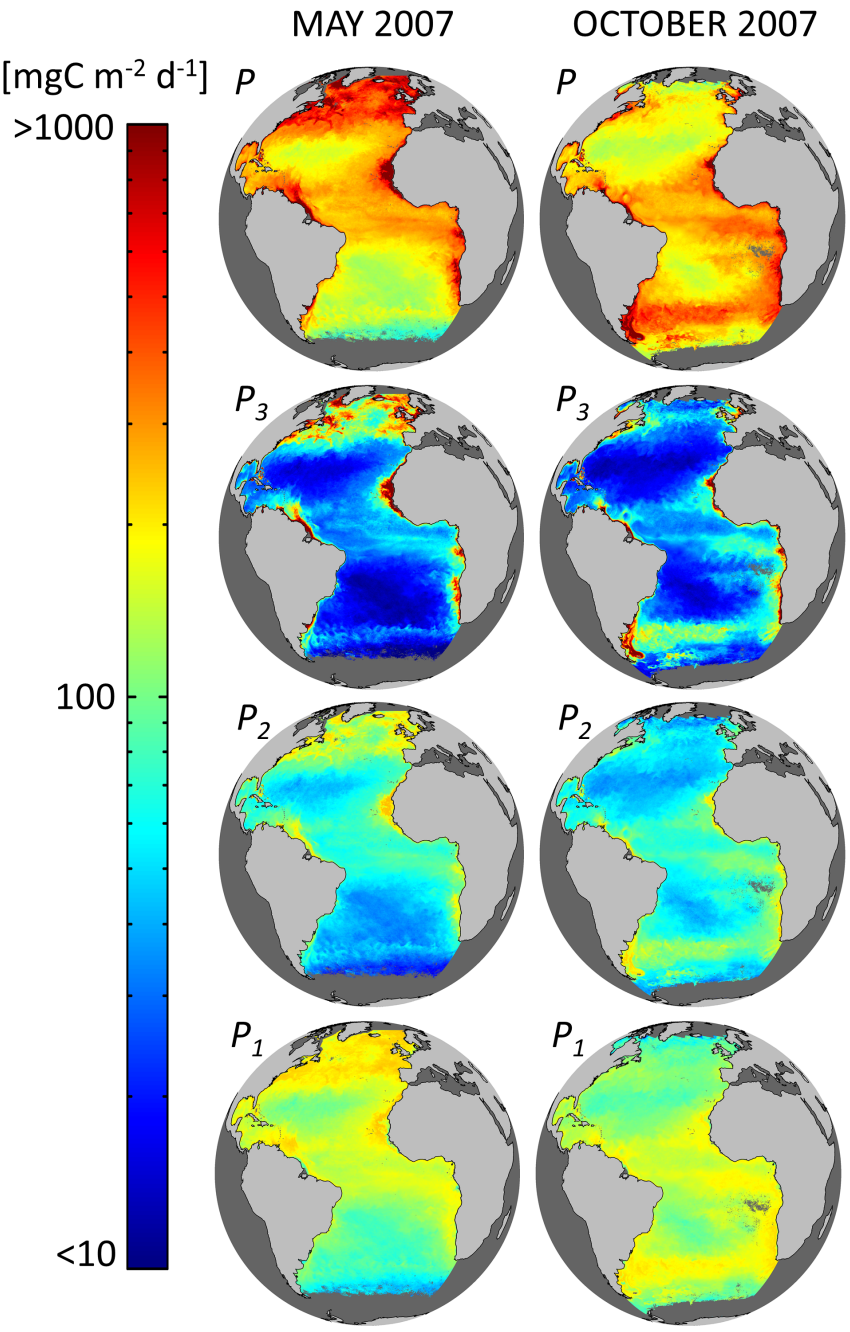

Figure 13: Total primary production (P), and primary production for small ($< 2\mu$m, denoted P_1), medium ($2 - 10\mu$m, denoted P_2) and large ($> 10\mu$m, denoted P_3) cells, for May and October 2007, in the Atlantic Ocean.

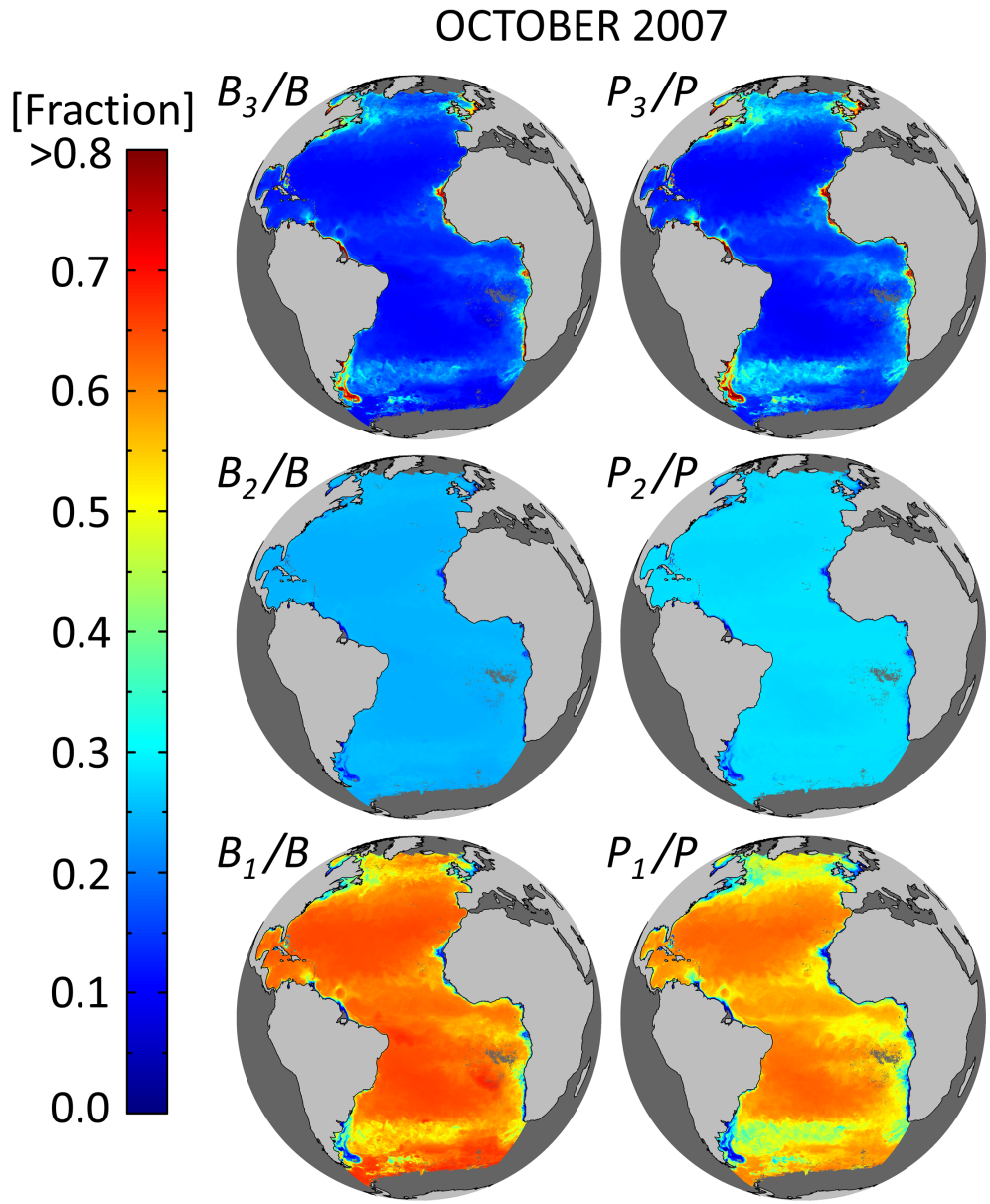

Figure 14: The fractional contribution of small ($< 2\mu$m, subscript $i = 1$), medium ($2 - 10\mu$m, subscript $i = 2$) and large ($> 10\mu$m, subscript $i = 3$) cells to total primary production (P) and depth-integrated chlorophyll biomass (denoted by B in this figure), for October 2007 in the Atlantic Ocean.

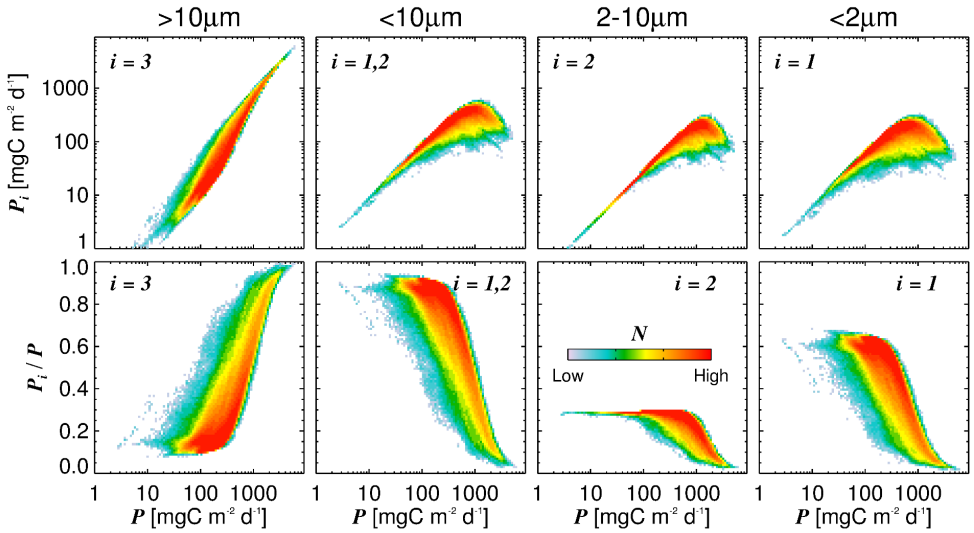

Figure 15: Size-fractionated primary production (P_i) plotted as a function of the total primary production (P) in the top row, with the fractions of each size class to total primary production (P_i/P) plotted as a function of the total primary production (P) in the bottom row. Data are from monthly satellite images of the Atlantic Ocean in 2007. Colour-bar represents a density scale, from a low to a high number of observations.

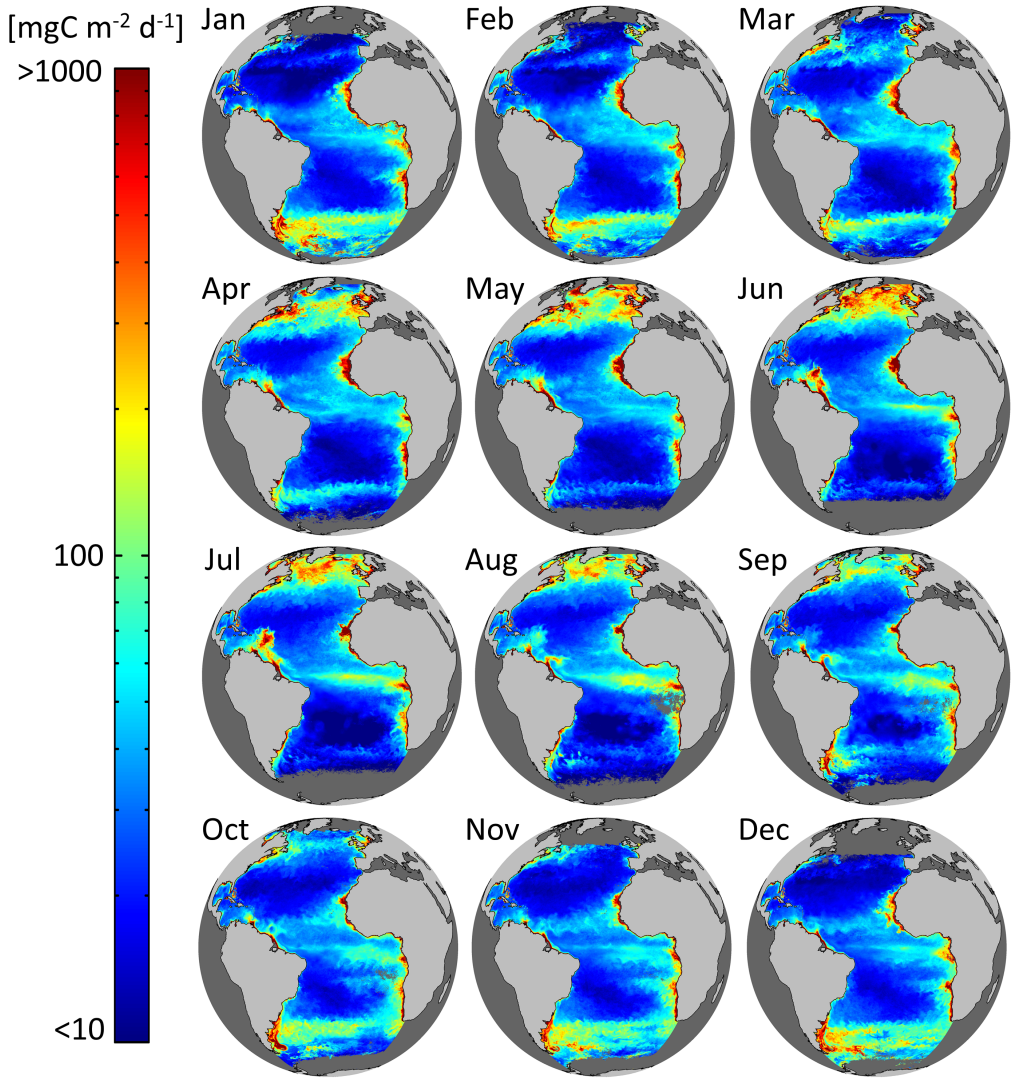

Figure 16: Daily primary production for large (> 10μm) cells for each month in 2007 in the Atlantic Ocean. Whereas we apply the model to monthly images in this figure, it has been parameterised using data collected principally between September and December.

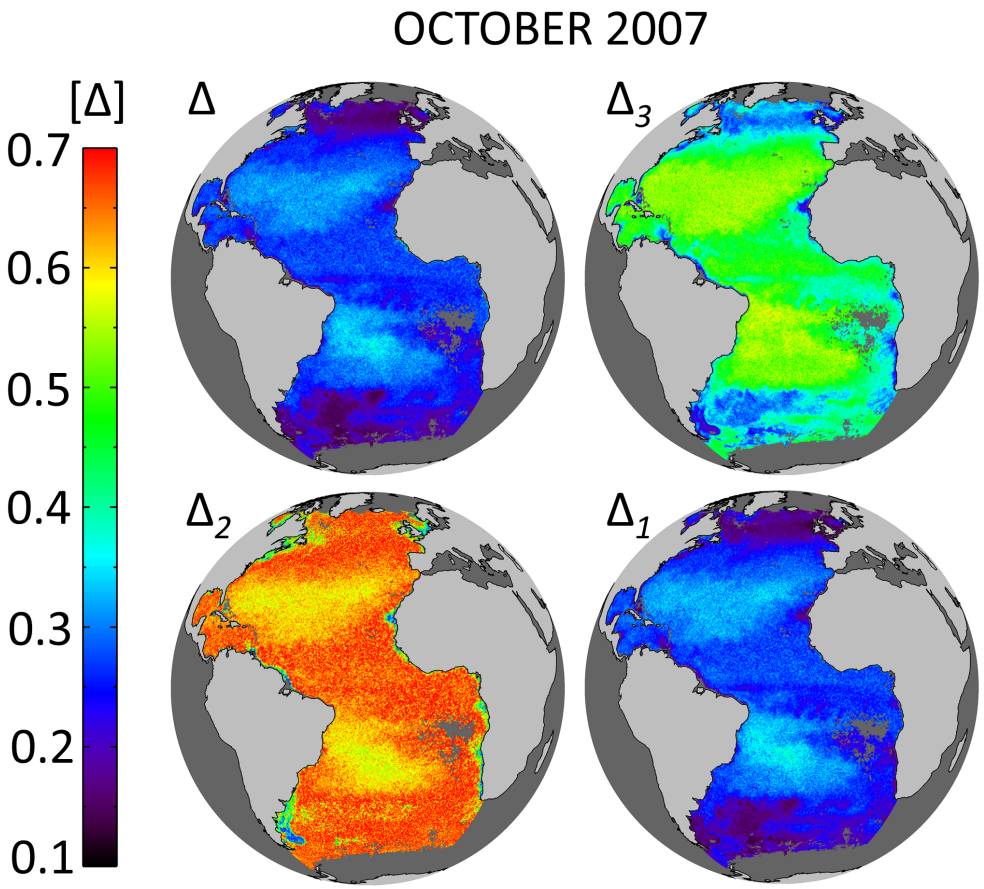

Figure 17: Estimates of the standard deviation in $\log_{10}$ total production (Δ), production by small cells (Δ_1), production by medium cells (Δ_2) and production by large cells (Δ_3), in the Atlantic Ocean for October 2007 from Monte Carlo simulations.

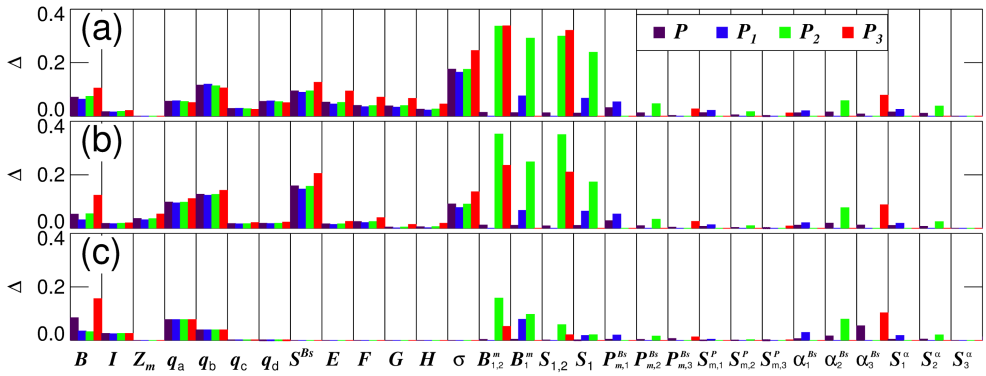

Figure 18: Sensitivity of model output (standard deviation in $\log_{10}$ production, denoted Δ) for total production (P) and that of the three size classes (P_1, P_2, P_3), when varying each input and parameter individually (using 200 random Monte Carlo simulations) whilst keeping the remaining values fixed. (a) Shows an oligotrophic case in the South Atlantic Gyre on the 10$^{\text{th}}$ January (latitude = $-20°$, longitude = $-30°$, $B = 0.05\,\text{mg}\,\text{m}^{-3}$, $I = 55$ Einstein $\text{m}^{-2}\,\text{d}^{-1}$ and $Z_m = 30\,\text{m}$); (b) a mesotrophic case in the equatorial Atlantic on the 19$^{\text{th}}$ August (latitude = $0°$, longitude = $-30°$, $B = 0.2\,\text{mg}\,\text{m}^{-3}$, $I = 40$ Einstein $\text{m}^{-2}\,\text{d}^{-1}$ and $Z_m = 50\,\text{m}$); and (c) a well-mixed eutrophic case in the North Atlantic on the 10$^{\text{th}}$ April (latitude = $45°$, longitude = $-30°$, $B = 2.0\,\text{mg}\,\text{m}^{-3}$, $I = 10$ Einstein $\text{m}^{-2}\,\text{d}^{-1}$ and $Z_m = 100\,\text{m}$).